Strain stiffening retards growth instability in residually stressed biological tissues

Yafei Wang [a,1], Yangkun Du [b,1], Fan Xu [a,*]

[a] *Institute of Mechanics and Computational Engineering, Department of Aeronautics and Astronautics, Fudan University, Shanghai, 200433, China*
[b] *School of Mathematics and Statistics, University of Glasgow, Glasgow, G128QQ, UK*

ARTICLE INFO

ABSTRACT

Soft biological tissues often exhibit notable strain stiffening under increasing stretch, and this can have significant effects on tissue growth and morphological development, such as causing symmetry breaking in growing airways and leading to mucosal folding and airway hyperresponsiveness. To investigate the role of strain stiffening and the multifactorial control in growth and remodeling, we consider a growing tubular structure with strain-stiffening effects caused by increased and tightened collagen. In addition, we employ the nonlinear hyperelastic Gent model and initial stress symmetry theory to include the coupling effects of differential growth and initial residual stress. Results show that for strain stiffening that takes place at higher strain ($\mathcal{J}_m > 21$), the maximum critical growth ratio matches that obtained using neo-Hookean model calculations. Meanwhile, for biological tissues that exhibit strain stiffening under moderate strain conditions ($0.46 < \mathcal{J}_m < 21$), the strain-stiffening effect delays significantly the onset of growth instability. When strain stiffening takes place at very low strains ($\mathcal{J}_m < 0.46$), stiff biological tissues can prevent growth instability, resulting in a smooth hyperelastic cylindrical tubular structure, and the epithelial tissue remains stable at all growth stages without forming any unstable morphology. Our results suggest that strain stiffening can induce retardation instability during biological growth and remodeling, but airway remodeling can incorporate this effect by increasing wall stiffness and reducing obstruction. This highlights the importance of considering the impact of strain stiffening on biological growth and remodeling, which can inform the development of effective clinical interventions for chronic inflammatory airway diseases.

1. Introduction

Embryonic development is driven by growth and remodeling processes (Taber, 1995), which can be characterized by external variations in mass and morphology as well as internal changes in local stress and strain distributions. These variations are influenced by endogenous factors such as gene expression (Rolland-Lagan et al., 2003) and cellular division, enlargement, death, shrinkage, and resorption (Xu et al., 2022), as well as exogenous factors such as biological environments (Dumais, 2007; Xu et al., 2020) and multiphysical loads in vivo (Xue et al., 2016). Developing a methodology for tissue growth has been a long-standing challenge, with the aim of accurately reproducing the intricate growth process and considering the influences of complex physical fields and
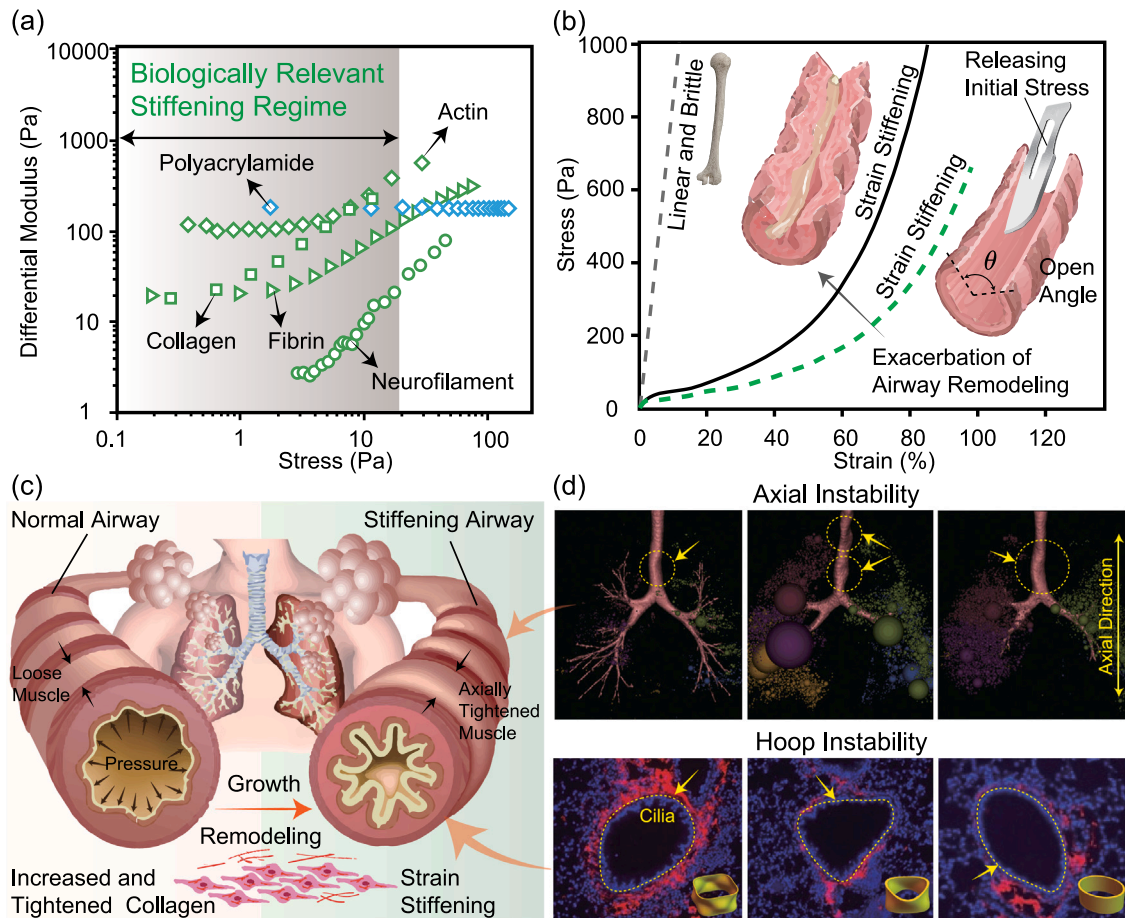

Fig. 1. (a) Schematic of differential modulus as a function of stress for intracellular and extracellular filamentous biopolymer materials exhibiting nonlinear stiffening effects, adapted from Das et al. (2016). (b) Stress–strain data for airway ring with different strain-stiffening levels (Jamieson et al., 2021). Releasing the initial residual stress in the airway is necessary for each measurement of the experimental curve. (c) Strain-stiffening effect of collagen increase in airway remodeling. (d) Visual representation of CT slices for airway remodeling (Xia et al., 2021; Doherty et al., 2011) demonstrating axial growth instability and hoop growth instability. In addition, the illustrations in this paper include three representative growth instability patterns that are calculated in airway remodeling and compared with CT images.

biomaterial properties. One feasible approach is to introduce a virtual incompatible state and separate the growth field from the entire growth process. Using the Kröner–Lee decomposition, Rodriguez et al. (1994) first developed a volume growth theory that describes the growth of biological tissues as a process of generating local strain incompatibility and repairing global elastic self-integrity. This model accurately captures the local incompatibility in the volume growth processes by assuming an appropriate local cumulative growth tensor, which is often a constant value or an experimentally derived function (Dervaux and Amar, 2011; Budday et al., 2014). However, as well as depending on the form of the growth tensor, local incompatibility is also associated with inhomogeneous growth (Fuiman, 1983; Amar and Goriely, 2005; Moulton and Goriely, 2011; Riccobelli and Bevilacqua, 2020; Lee et al., 2021; Wang et al., 2023), initial residual stress (Gower et al., 2015; Ciarletta et al., 2016; Du et al., 2018, 2019a; Ciarletta et al., 2022; Liu et al., 2022), and tissue nonlinearity [see Fig. 1(a) and (b) for details] (Storm et al., 2005; Destrade et al., 2009; Sharma et al., 2016; Vatankhah-Varnosfaderani et al., 2017; Weickenmeier et al., 2018).

Inhomogeneous growth can result from differential and anisotropic growth, leading to the formation of complex folding patterns in a unidirectional manner. For example, human and chick guts both exhibit cylindrical shapes at the primitive midgut stage (Shyer et al., 2013). During growth, the endoderm and mesenchymal layers become intertwined (Ben Amar and Jia, 2013), and the previously formed circumferential ridges collapse into parallel zigzags due to longitudinal muscle development. Columnar microstructures of villi are produced through the coalescence of surface patterns (Ciarletta et al., 2014). Smooth muscle differentiation is strongly connected to epithelial morphogenesis, which is heterogeneous, anisotropic, and constrained by boundary conditions, as evidenced by the presence of circumferential folds, longitudinal instability, and previlli. Regarding inhomogeneous growth models, they can be split into two classes. The first class involves micro-structures, such as longitudinal fibers, that determine the preferred direction for growth; this approach involves constructing a growth tensor aligned with the orientation of the fibers and has been used to explain the formation of brain cortical wrinkles and other fibrous structures (Lubarda and Hoger, 2002; Menzel,

2005; Bayly et al., 2014). The second class considers intrinsic nonhomogeneity resulting from anisotropic elastic stiffness (Braeu et al., 2019; Soleimani et al., 2020); in this approach, the shape of the growth tensor is determined by the compliance tensor, and growth tends to occur in the directions of lowest stiffness.

In addition to inhomogeneous growth, experiments have shown that biological tissues often have initial residual stresses that are difficult to unload completely, and these initial residual stresses can significantly affect the further growth and morphology evolution processes. However, limited by the assumption of unrestricted growth, the initial configuration of biological tissues must be stress-free. To consider the influence of initial stress, a modified multiplicative decomposition growth model (Du et al., 2018) based on initial stress symmetry (Gower et al., 2015; Ciarletta et al., 2016) has been proposed. This initial stress symmetry restricts the constitutive form of the Cauchy stress by providing a constitutive equation for the initial stress, allowing the depiction of the free energy density as a function of the initial stress and deformation gradient tensor (Skalak et al., 1996; Hoger, 1997). Moreover, polymer experiments (Du et al., 2019b) have shown that it is practically feasible for different target topologies to be obtained by using prescribed initial residual stress fields or initial geometries.

It is important to acknowledge that the majority of biological tissues – such as blood vessels, corneas, lung tissue, mesentery, clots, actin, collagen, fibrin, and neurofilaments – are not homogeneous and linear elastic materials. Instead, they exhibit a significant increase in stiffness that is related nonlinearly to strain [see Fig. 1(a) and (b) for more information]. This strain-stiffening effect results from the tightening, rotation, and increase of fibers in the direction of loading and is an inherent feature of biological self-protection that is not easily reproduced in synthetic materials (Wang and Wang, 2021, 2022; Kouwer et al., 2013; Jaspers et al., 2014). At the cellular level, these biomaterials also exhibit strain-stiffening effects, which can influence the differentiation of stem cells. Simply altering the strain-stiffening parameter can transform human mesenchymal stem cells from adipogenesis to osteogenesis (Das et al., 2016). In addition, there is continuous research fervor about the growth and remodeling of biologically relevant strain-stiffening effects because of their applications in biomedical engineering (Vatankhah-Varnosfaderani et al., 2017; Rodrigo-Navarro et al., 2021). Several theoretical studies have shed light on the complex mechanics of tissue nonlinearity, emphasizing the significance of the tissue microstructure in growth and remodeling. For example, Storm et al. (2005) investigated the strain stiffening of bionic gels and identified the critical role played by semiflexible polymer networks in tissue growth. Similarly, Sharma et al. (2016) demonstrated that the nonlinear behavior of active fiber networks is governed by strain-controlled criticality, which is a crucial mechanism in tissue remodeling. Furthermore, Weickenmeier et al. (2018) studied the post-mortem stiffening of brain tissue, which involves the loss of water and ions as well as changes in tissue microstructure, highlighting the importance of understanding the tissue growth and remodeling processes. Despite these efforts, the level to which strain stiffening can affect biological growth and remodeling is still unknown. To the best of our knowledge, the effects of strain stiffening on the mechanics of growth instability have not been examined in the context of volumetric growth, and there has been relatively little research on the synergistic mechanics of growth that involve inhomogeneous growth, initial stress and, strain stiffening.

Therefore, constructing a free energy density and Cauchy stress that account for tissue growth and remodeling – including the strain-stiffening effect and initial residual stress field – presents a challenge. In this study, we focus on the residual stress and morphology alterations of airway growth and remodeling [see Fig. 1(c) and (d) for details], with the aim of exploring the relevance of strain stiffening and initial stress (Black et al., 2001; Tagaya and Tamaoki, 2007) for various chronic inflammatory airway diseases (Hirota and Martin, 2013). Existing evidence shows that increased and tightened collagen in the airway can lead to strain stiffening and airway hyperresponsiveness, contributing to airway remodeling. Mucosal folding and symmetry breaking are indicators of disease progression (Mostaço-Guidolin et al., 2019; Hough et al., 2020; Varricchi et al., 2022).

From a modeling perspective, we model the airway as a single-layer incompressible hyperelastic tube (i.e., intertwined mucus, cilia, and smooth muscle layers) with variable thickness and a certain initial residual stress (Goriely, 2017). We assume that the tube undergoes differential growth in the principal directions, and we use nonlinear elasticity and field theory to calculate the deformed configuration and residual stresses. In addition, to explore the role of nonlinear strain stiffening and the multifactorial control in airway remodeling and instability, we perform linear incremental analysis. Despite not examining subcellular structures, this work provides mechanistic knowledge and predictive insights into airway remodeling and its quantification.

The paper is organized as follows. In Section 2, we model tissue growth by the triphasic decomposition of the total deformation gradient, and the Cauchy stress is derived. In Section 3, we explain the ground state structure and provide the equations for initial residual stress, deformation, and Cauchy stress. In Section 4, we cover the bifurcation problem in the Stroh formulation and derive the generalized incremental equations governing symmetry breaking. In Section 5, we discuss numerical results and further refine retardation growth instability induced by strain stiffening. Finally, in Section 6 we draw conclusions and highlight the significant implications of this research for airway remodeling. The specific Stroh matrix and results for growing cylinders with strain-stiffening effects can be found in the Supplementary material.

2. Triphasic decomposition growth model

We consider the growth of a residually stressed strain-stiffening solid subjected to external loads, where the position vector $\mathbf{X}$ in the reference configuration $\mathcal{B}_r$ is deformed to $\mathbf{x}$ in the current configuration $\mathcal{B}_c$. To describe this deformation, we define the invertible motion function $\mathbf{x} = \chi(\mathbf{X}, t)$, which maps $\mathbf{X}$ to $\mathbf{x}$. Therefore, the deformation gradient tensor is given by the gradient of the motion function, $\mathbf{F}(\mathbf{X}, t) = \text{Grad} \chi$, and the Jacobian transformation, $J(\mathbf{X}, t) = \det \mathbf{F}(\mathbf{X}, t)$, which must be positive for all deformations. To address the coupling effects of initial stress in growth, as illustrated in Fig. 2(a), we use the triphasic decomposition growth model $\mathbf{F} = \mathbf{AGS}$, where the initial elastic deformation tensor $\mathbf{S}$ creates an intermediate stress-free configuration, $\bar{\mathcal{B}}_s$, the growth tensor $\mathbf{G}$ transforms $\bar{\mathcal{B}}_s$ into the virtual growth configuration $\bar{\mathcal{B}}_g$, and $\mathbf{A}$ forms $\mathcal{B}_c$ from disconnected components in $\bar{\mathcal{B}}_g$.
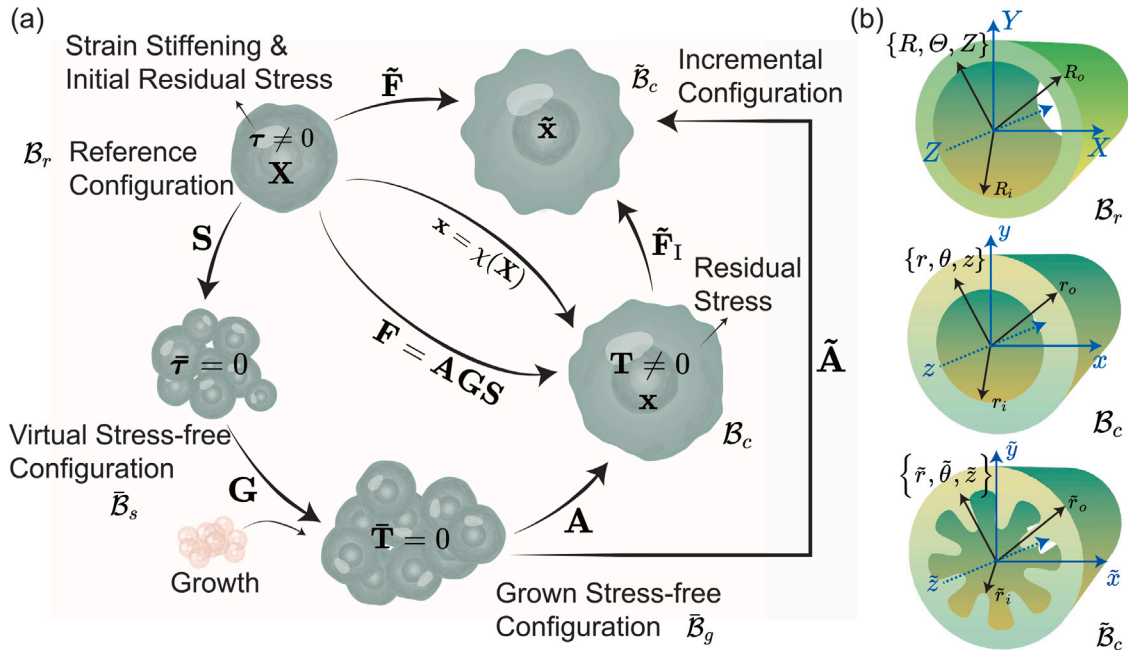
Fig. 2. (a) Evolution of initially residually stressed configuration with strain stiffening, and diagram of multiplicative decomposition for growing matter. (b) Geometrical description of initially residually stressed cylindrical tubes with strain-stiffening effect.

Based on the triphasic multiplicative decomposition, using two different virtual stress-free configurations $\bar{\mathcal{B}}_s$ and $\bar{\mathcal{B}}_g$ as a starting point, we can investigate the fundamental connections among strain stiffening, initial residual stress, growth, and instability.

The Jacobian transformations associated with the various deformation gradients are given by $J_s = \det \mathbf{S}$, $J_g = \det \mathbf{G}$, and $J_a = \det \mathbf{A}$, respectively. For incompressible materials, we have $J_s = 1$, $J_a = 1$, and $J = J_g$. Considering the internal material constraints of a hyperelastic solid, we can modify the strain energy function Ψ using $\Psi \to \Psi - qC$ (C is a smooth scalar function). Therefore, the energy balance equation is $\mathrm{tr}((\partial(\Psi - qC)/\partial \mathbf{F} - \mathbf{P})\dot{\mathbf{F}}) = 0$, where q is the Lagrangian multiplier, $\mathbf{P}$ is the first Piola–Kirchhoff stress tensor, and the superposed dot represents the material time derivative. Correspondingly, $\mathbf{T}$ represents the Cauchy stress tensor. For incompressible hyperelastic materials with volumetric growth, all elastic deformations must preserve volume, meaning that $C = J_a - 1$. The energy balance equation shows that the first Piola–Kirchhoff stress tensor and the Cauchy stress tensor are

$$\mathbf{P} = J\frac{\partial \Psi}{\partial \mathbf{F}} - qJ\frac{\partial C}{\partial \mathbf{F}} = J\mathbf{S}^{-1}\mathbf{G}^{-1}\frac{\partial \Psi}{\partial \mathbf{A}} - qJ\mathbf{F}^{-1} \text{ and } \mathbf{T} = \mathbf{A}\frac{\partial \Psi}{\partial \mathbf{A}} - q\mathbf{I}. \tag{1}$$

If there is no body force, then the first Cauchy equations reduce to

$$\mathrm{div}(\mathbf{T}) = \mathbf{0} \text{ and } \mathrm{Div}(\mathbf{P}) = \mathbf{0}, \tag{2}$$

where div and Div are taken in $\mathcal{B}_r$ and $\mathcal{B}_c$, respectively. Assuming that the strain energy function of an initially stressed hyperelastic material is of the form $\Psi = \Psi(\mathbf{A})$, we have the first Piola–Kirchhoff stress and Cauchy stress as

$$\mathbf{P} = \hat{\mu}J\mathbf{S}^{-1}\mathbf{G}^{-1}\mathbf{G}^{-T}\mathbf{S}^{-T}\mathbf{F}^{T} - qJ\mathbf{F}^{-1} \text{ and } \mathbf{T} = \hat{\mu}\mathbf{F}\mathbf{S}^{-1}\mathbf{G}^{-1}\mathbf{G}^{-T}\mathbf{S}^{-T}\mathbf{F}^{T} - q\mathbf{I}, \tag{3}$$

where $\hat{\mu}$ is the generalized shear modulus function, with $\hat{\mu} = \mu$ for a neo-Hookean material. For hyperelastic materials with strain-stiffing effects, such as the Gent materials, we have the deformation-related $\hat{\mu} = \mu \mathcal{J}_m/(\mathcal{J}_m - (\mathbf{C}_a : \mathbf{I} - 3))$, where $\mathcal{J}_m$ is the strain stiffening level and $\mathbf{C}_a = \mathbf{A}^{T}\mathbf{A}$ is the right Cauchy–Green tensor.

With respect to axisymmetric growth, we assume that the deformation gradient tensor $\mathbf{F}$ and growth tensor $\mathbf{G}$ are diagonal matrices. Hence, using the commutativity of multiplication, the first Piola–Kirchhoff stress $\mathbf{P}$ and Cauchy stress $\mathbf{T}$ according to Eq. (3) can be rewritten as

$$\mathbf{P} = \hat{\mu}J\mathbf{B}_g^{-1}\mathbf{B}_0^{(-1)}\mathbf{F}^{T} - qJ\mathbf{F}^{-1} \text{ and } \mathbf{T} = \hat{\mu}\mathbf{B}_g^{-1}\mathbf{B}_0^{(-1)}\mathbf{B} - q\mathbf{I}, \tag{4}$$

where $\mathbf{B}_0^{(-1)} = \mathbf{S}^{-1}\mathbf{S}^{-T}$, $\mathbf{B}_g = \mathbf{G}\mathbf{G}^{T}$, and $\mathbf{B} = \mathbf{F}\mathbf{F}^{T}$. Under the guidance of the commutativity, the linked theoretical treatment enables us to forecast the initial elastic deformation. From configuration $\bar{\mathcal{B}}_s$ to $\mathcal{B}_r$ and using $\tau = \mathbf{T}(\mathbf{G} = \mathbf{I}, \mathbf{F} = \mathbf{I})$, the initial residual stress tensor τ and the initial elastic deformation tensor $\mathbf{B}_0^{(-1)}$ are given by

$$\tau = \hat{\mu}\mathbf{B}_0^{(-1)} - q_0\mathbf{I} \text{ and } \mathbf{B}_0^{(-1)} = (\tau + q_0\mathbf{I})/\hat{\mu}, \tag{5}$$

where q_0 is the Lagrangian multiplier in $\mathcal{B}_r$.

The Gent model is one of the best-known constitutive laws that can feature the strain-stiffening effect of biological tissues. Its strain energy function is of the form $\Psi = -\frac{\mu \mathcal{J}_m}{2} \ln(1 - (\mathbf{C}_a : \mathbf{I} - 3)/\mathcal{J}_m)$, where $\mathcal{J}_m > 0$ describes the finite extensibility of the chains, which reflects the singular limit of the strain energy function. As the strain stiffening level $\mathcal{J}_m$ approaches infinity, the Gent model converges to the neo-Hookean model. For an incompressible Gent material, Eq. (5) can be expressed as

$$\boldsymbol{\tau} = \frac{\mu \mathcal{J}_m}{\mathcal{J}_m - (\mathrm{tr}(\mathbf{B}_0^{(-1)}) - 3)} \mathbf{B}_0^{(-1)} - q_0 \mathbf{I}, \tag{6}$$

by which we can obtain

$$\mathbf{B}_0^{(-1)} = \frac{(\mathcal{J}_m + 3)(\boldsymbol{\tau} + q_0 \mathbf{I})}{\mu \mathcal{J}_m + 3q_0 + \mathrm{tr}(\boldsymbol{\tau})}. \tag{7}$$

Note that when $\mathcal{J}_m \to \infty$, the initially residually stressed deformation $\lim_{\mathcal{J}_m \to \infty} \mathbf{B}_0^{(-1)} = (\boldsymbol{\tau} + q_0 \mathbf{I})/\mu$ allows us to recover the case of initially stressed neo-Hookean materials. Moreover, recall that the material is incompressible, so the deformations $\mathbf{S}^{-1}$ and $\mathbf{B}_0^{(-1)}$ are isochoric, which implies

$$\det\left(\frac{\mu \mathcal{J}_m + 3q_0 + I_{\tau_1}}{\mathcal{J}_m + 3} \mathbf{B}_0^{(-1)}\right) = \left(\frac{\mu \mathcal{J}_m + 3q_0 + I_{\tau_1}}{\mathcal{J}_m + 3}\right)^3 = \det(\boldsymbol{\tau} + q_0 \mathbf{I}). \tag{8}$$

Thus, q_0 can be obtained by solving the cubic equation

$$q_0^3 + q_0^2 I_{\tau_1} + q_0 I_{\tau_2} + I_{\tau_3} = \left(\frac{\mu \mathcal{J}_m + 3q_0 + I_{\tau_1}}{\mathcal{J}_m + 3}\right)^3, \tag{9}$$

where $I_{\tau_1} = \mathrm{tr}(\boldsymbol{\tau})$, $I_{\tau_2} = \frac{1}{2}\left(\mathrm{tr}(\boldsymbol{\tau})^2 - \mathrm{tr}(\boldsymbol{\tau}^2)\right)$, and $I_{\tau_3} = \det(\boldsymbol{\tau})$ are three invariants of the initial residual stress tensor $\boldsymbol{\tau}$. Note that identifying the Lagrangian multiplier in a cubic equation requires all three components of the initial residual stress tensor. Note also that when $\mathcal{J}_m \to \infty$, q_0 is actually the exact solution of $q_0^3 + q_0^2 I_{\tau_1} + q_0 I_{\tau_2} + I_{\tau_3} = \mu^3$.

3. Growth of incompressible strain-stiffening biological tubular structure

3.1. Modeling finite deformation

As illustrated in Fig. 2(b), for the reference configuration without growth deformation, the radius and axial length of the biological tubular structure fall within the intervals $R_i \leqslant R \leqslant R_o$ and $0 \leqslant Z \leqslant L$, respectively. We consider a residually stressed cylindrical tube with axisymmetric deformation, and we assume an axial initial stress field with components

$$\tau_{RR} = \alpha \mu \ln \frac{R}{R_i} \ln \frac{R}{R_o}, \quad \tau_{\Theta\Theta} = \alpha \mu \ln \frac{R^2}{R_i R_o} + \alpha \mu \ln \frac{R}{R_i} \ln \frac{R}{R_o}, \quad \tau_{ZZ} = \alpha \mu R - \frac{2\alpha \mu \left(R_i^2 + R_i R_o + R_o^2\right)}{3\left(R_i + R_o\right)}, \tag{10}$$

where $\tau_{ZZ} = \mu(\alpha R + \beta)$ is assumed to be distributed linearly in the radial direction and satisfies the zero-traction condition $2\pi \int_{R_i}^{R_o} R \tau_{ZZ} \, dR = 0$. Considering the growth of a tube in cylindrical coordinates [see Fig. 2(b)], we have the total deformation $\mathbf{F} = \mathrm{diag}\left(\partial r(R)/\partial R, r(R)/R, \lambda_3\right)$, where $\lambda_3 = l/L$ is the stretch ratio in the axial direction. In addition, we assume the growth tensor $\mathbf{G} = \mathrm{diag}(g_1, g_2, g_3)$. Then, the incompressibility condition can be expressed as

$$\det\left(\mathbf{F}\mathbf{S}^{-1}\mathbf{G}^{-1}\right) = 1 \Rightarrow r^2 = r_i^2 + 2\int_{R_i}^{R} \lambda_3^{-1} J_g(R) \, R \, dR, \tag{11}$$

where $r_i = r(R_i)$ and $r_o = r(R_o)$. If the growth factors are independent of the deformation, then we have $r^2 = r_i^2 + \lambda_3^{-1} J_g(R^2 - R_i^2)$. According to Eqs. (4)$_2$ and (7), the Cauchy stress components in the tube are

$$
\begin{aligned}
T_{rr} &= \frac{\mu \mathcal{J}_m (\mathcal{J}_m + 3)(\tau_{RR} + q_0)\left(\frac{Rg_2 g_3}{r\lambda_3}\right)^2}{(\mathcal{J}_m - \mathrm{tr}(\mathbf{C}_a) + 3)(\mu \mathcal{J}_m + 3q_0 + \tau_{RR} + \tau_{\Theta\Theta} + \tau_{ZZ})} - q, \\[2mm]
T_{\theta\theta} &= \frac{\mu \mathcal{J}_m (\mathcal{J}_m + 3)(\tau_{\Theta\Theta} + q_0)\left(\frac{r}{g_2 R}\right)^2}{(\mathcal{J}_m - \mathrm{tr}(\mathbf{C}_a) + 3)(\mu \mathcal{J}_m + 3q_0 + \tau_{RR} + \tau_{\Theta\Theta} + \tau_{ZZ})} - q, \\[2mm]
T_{zz} &= \frac{\mu \mathcal{J}_m (\mathcal{J}_m + 3)(\tau_{ZZ} + q_0)\left(\frac{\lambda_3}{g_3}\right)^2}{(\mathcal{J}_m - \mathrm{tr}(\mathbf{C}_a) + 3)(\mu \mathcal{J}_m + 3q_0 + \tau_{RR} + \tau_{\Theta\Theta} + \tau_{ZZ})} - q,
\end{aligned}
\tag{12}
$$

with the trace of the right Cauchy–Green tensor being

$$\mathrm{tr}(\mathbf{C}_a) = \frac{\mathcal{J}_m + 3}{\mu \mathcal{J}_m + 3q_0 + \tau_{RR} + \tau_{\Theta\Theta} + \tau_{ZZ}} \left(\frac{(\tau_{RR} + q_0) R^2 g_2^2 g_3^2}{r^2 \lambda_3^2} + \frac{(\tau_{\Theta\Theta} + q_0) r^2}{R^2 g_2^2} + \frac{(\tau_{ZZ} + q_0) \lambda_3^2}{g_3^2}\right). \tag{13}$$

Note that when $\mathcal{J}_m \to \infty$, the current Cauchy stress tensor recovers the case of the neo-Hookean model, i.e., $\mathbf{T} = \mathbf{B}_g^{-1}(\boldsymbol{\tau} + q_0 \mathbf{I})\mathbf{B} - q\mathbf{I}$.
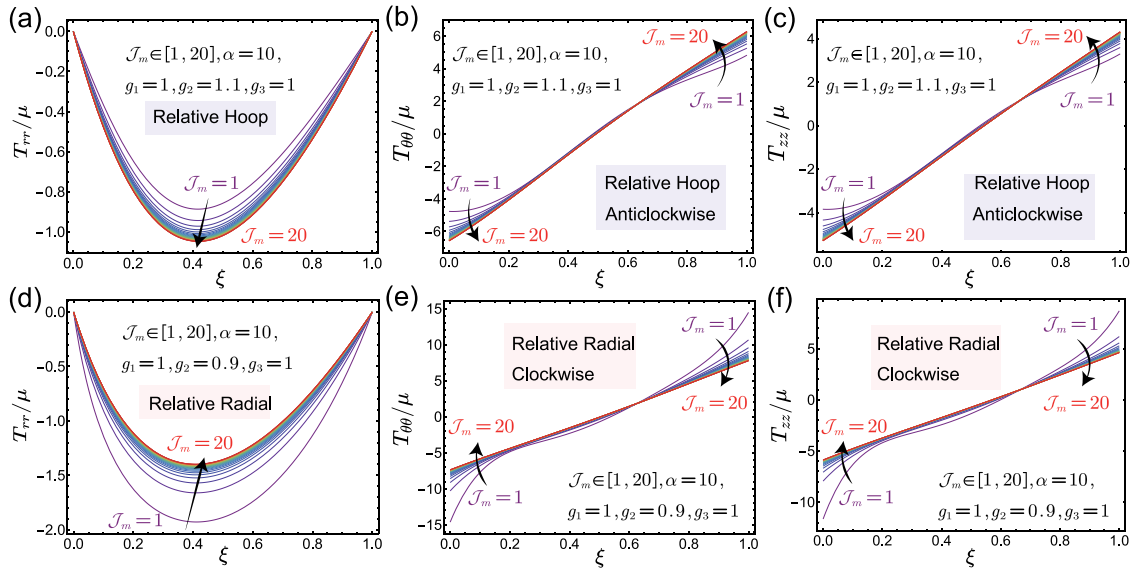
Fig. 3. Effects of strain stiffening on growth-induced residual stress: (a) T_{rr}/μ, (b) $T_{\theta\theta}/\mu$, and (c) T_{zz}/μ as functions of dimensionless ξ for relative hoop growth $g_2/g_1 = 1.1$, strain-stiffening parameter $1 \leqslant \mathcal{J}_m \leqslant 20$, and $Q = 0, \alpha = 10, g_3 = 1, \lambda_3 = 1$; (d) T_{rr}/μ, (e) $T_{\theta\theta}/\mu$, and (f) T_{zz}/μ as functions of dimensionless ξ for relative radial growth $g_2/g_1 = 0.9$, strain-stiffening parameter $1 \leqslant \mathcal{J}_m \leqslant 20$, and $Q = 0, \alpha = 10, g_3 = 1, \lambda_3 = 1$.

For axisymmetric deformation, the first Cauchy equation $\text{div}(\mathbf{T}) = \mathbf{0}$ reduces to

$$\frac{\partial T_{rr}}{\partial r} + r^{-1}(T_{rr} - T_{\theta\theta}) = 0. \tag{14}$$

Using $r dr = R\lambda_3^{-1} J_g H d\xi$ and $H = R_o - R_i$, we reformulate the boundary condition as

$$\int_0^1 \frac{H\left(\xi H + R_i\right)\lambda_3^{-1} J_g \left(T_{\theta\theta} - T_{rr}\right)}{r_i^2 + \lambda_3^{-1} J_g \xi H \left(\xi H + 2R_i\right)} d\xi = Q, \tag{15}$$

where Q is the internal pressure. Moreover, the integral condition for the end caps of the tube can be given by

$$\pi \int_0^1 H\left(\xi H + R_i\right)\lambda_3^{-1} J_g \left(2T_{zz} - T_{\theta\theta} - T_{rr}\right) d\xi = 0. \tag{16}$$

Once r_i is determined by using the explicit Newton method on Eqs. (15) and (16), we can obtain the Cauchy stress components according to Eq. (12).

3.2. Effects of strain stiffening on basic state

In a simple extension experiment, a Gent material becomes increasingly difficult to stretch further, and there is a maximum stretch given by $\lambda_{\max}^2 + 2/\lambda_{\max} = \mathcal{J}_m + 3$. For example, the arteries of a young human can be stretched up to a value of $\lambda_{\max} = 1.4$ (i.e., $\mathcal{J}_m = 0.38857$), while those of a 70-year-old human can be stretched only up to $\lambda_{\max} = 1.2$ (i.e., $\mathcal{J}_m = 0.10667$). For arteries, the representative range of the stiffening parameter (Destrade et al., 2009) is $0.4 \leqslant \mathcal{J}_m \leqslant 2.3$, while for hyperelastic rubber it is $20 \leqslant \mathcal{J}_m \leqslant 200$.

In Fig. 3, we demonstrate the impact of strain stiffening on a growing hyperelastic tube made from strain-stiffening material when the initial stress level is $\alpha = 10$ and the pressure is $Q = 0$. By comparing Fig. 3(a)–(c), we can infer that for $1 \leqslant \mathcal{J}_m \leqslant 20$ and a relative hoop growth of $g_2/g_1 = 1.1$, the softer Gent materials exhibit lower Cauchy stress for T_{rr}. It is interesting to note that the Cauchy stresses for $T_{\theta\theta}$ and T_{zz} show an anticlockwise variation with respect to the increase of strain-stiffening level. Fig. 3(d)–(f) show the variations of radial T_{rr}, circumferential $T_{\theta\theta}$, and axial T_{zz} Cauchy stresses with dimensionless radius ξ for $\alpha = 10$, $1 \leqslant \mathcal{J}_m \leqslant 20$, and relative radial growth $g_2/g_1 = 0.9$. In particular, the numerical trend of the Cauchy stress against the dimensionless radius is similar to that of the relative hoop growth, while the softer Gent materials have higher growth-induced residual stresses for T_{rr}. In this situation, the Cauchy stresses for $T_{\theta\theta}$ and T_{zz} exhibit a clockwise trend concerning the increment of strain-stiffening level. These observations demonstrate directly that the basic state solutions of strain-stiffening biological tubular structures are significantly sensitive to differential growth and strain stiffening. In fact, when $\mathcal{J}_m \to \infty$, the material recovers into a neo-Hookean solid without strain stiffening.

Next, we use the developed strain-stiffening model to investigate the growth stability when the internal pressure Q is nonzero. For constrained axial stretch ($\lambda_3 = 1$), Fig. 4 shows the dimensionless Q/μ as a function of r_i/R_i. In Fig. 4(a), we observe that the
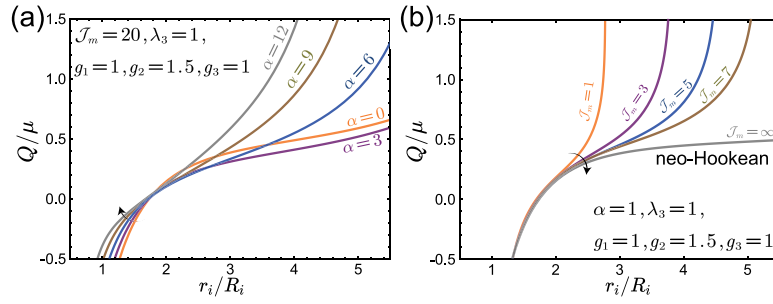
Fig. 4. Effects of strain stiffening on growing tube with internal pressure and constrained axial stretch $\lambda_3 = 1$ for (a) $\mathcal{J}_m = 20, g_2/g_1 = 1.5, 3 \leqslant \alpha \leqslant 12$ and (b) $\alpha = 1, g_2/g_1 = 1.5, 1 \leqslant \mathcal{J}_m \leqslant \infty$. Note that as the level of strain stiffening tends to infinity, the computation approaches the case of initially stressed neo-Hookean materials.
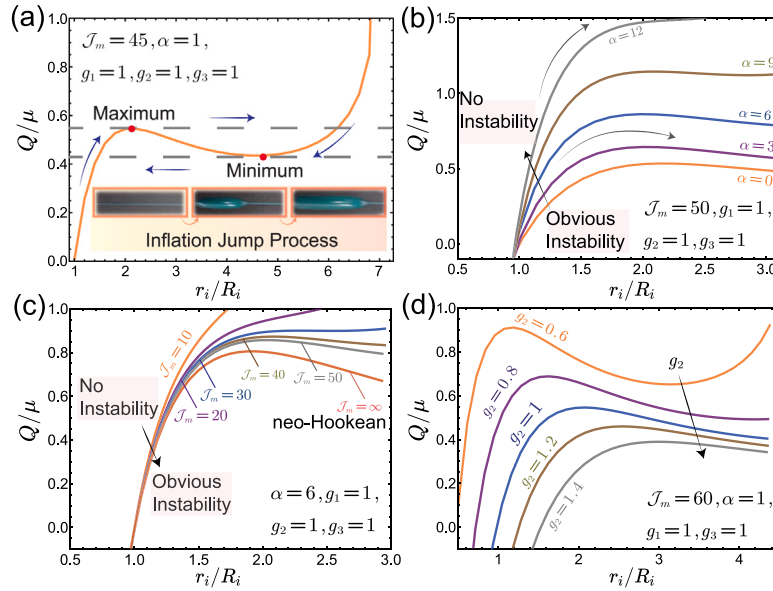

Fig. 5. Effects of strain stiffening on growing tube with internal pressure and unconstrained axial stretch: (a) monotonicity loss of pressure curve; (b) variation of pressure curves with changes in radius ratio for different initial stress levels while maintaining a constant strain-stiffening level $\mathcal{J}_m = 50$; (c) variation of pressure curves with changes in radius ratio for different strain-stiffening levels $10 \leqslant \mathcal{J}_m \leqslant \infty$; (d) evolution of pressure curves with changes in radius ratio for different growth factors while maintaining a constant strain-stiffening level $\mathcal{J}_m = 60$.

pressure curves undergo a sharp jump with increase of the initial residual stress amplitude α. Generally, when the radius ratio is less than 1.8, increasing the initial stress level leads to a decrease in the internal pressure. Conversely, when the radius ratio is greater than 1.8, increasing α results in larger Q, except for curves with $\alpha = 0$. For a fixed initial stress level $\alpha = 1$, the pressure curves show a similar behavior of limiting chain extensibility, as can be seen from Fig. 4(b). The inflection point is obvious for the smaller strain-stiffening parameter $\mathcal{J}_m$, and an increase in the level of strain stiffening results in a decrease in the internal pressure. These observations show the significant limiting chain extensibility and strain-stiffening effects, but they cannot involve the limiting-point instability phenomenon and inflation jump.

According to Fig. 5, growing cylindrical tubes with initial residual stress can in particular result in an inflation jump process because of the strain stiffening. This limit-point instability is caused by loss of monotonicity for the pressure curve, which in the case of a growing tube with strain stiffening has a local maximum followed by a minimum [see Fig. 5(a) for details]. The curves display hysteresis when subjected to controlled pressure. Decreased initial stresses clearly cause the limit-point instability shown in Fig. 5(b), and the stress-free initial configuration can experience hysteresis without differential growth. In Fig. 5(c), we plot the internal pressure Q/μ against r_i/R_i for different values of the stiffening parameter $\mathcal{J}_m \geqslant 10$. The localization of instability in the growing tube is hastened greatly by increasing the strain-stiffening parameter. For the fixed stiffening parameter $\mathcal{J}_m = 60$ in Fig. 5(d), differential growth from radial contraction $g_1 = 0.6$ to radial expansion $g_1 = 1.4$ is effective in decreasing the pressure and maintaining the limit-point instability and an inflation jump. We draw the conclusion that growth instability in the initially stressed tube is influenced significantly by the strain-stiffening effects.

4. Perturbation analysis for strain-stiffening biological tubular structure

4.1. Derivation of incremental equation

Leveraging the theory of superimposed incremental deformations, we characterize the bifurcation of the growing cylinder with initial residual stress and strain stiffening. As can be seen from Fig. 2, we assume that the base solutions for the Cauchy stress $\mathbf{T}^{(0)}$ and deformation $\chi^{(0)}$ are known, as are the boundary conditions. By introducing an increment $\chi^{(1)}$, we have the first-order kinematics $\tilde{\chi} = \chi^{(0)}(\mathbf{X}) + \varepsilon\chi^{(1)}(\mathbf{x})$, where ε is a small perturbation parameter. The geometric deformation gradient in $\tilde{B}_c$ can be calculated using the chain rule:

$$\tilde{\mathbf{F}} = \operatorname{Grad}\tilde{\chi} = \tilde{\mathbf{F}}_{\mathrm{I}}\mathbf{F}^{(0)} = \mathbf{F}^{(0)} + \varepsilon\tilde{\mathbf{F}}^{(0)}, \tag{17}$$

where $\tilde{\mathbf{F}}_{\mathrm{I}} = \mathbf{I} + \varepsilon\mathbf{F}^{(1)}$, $\tilde{\mathbf{F}}^{(0)} = \mathbf{F}^{(1)}\mathbf{F}^{(0)}$, and $\mathbf{F}^{(1)} = \operatorname{grad}(\chi^{(1)})$ is the associated incremental displacement gradient tensor. By taking the expansion of the pure elastic deformation tensor, we have $\tilde{\mathbf{A}} = \mathbf{A}^{(0)} + \varepsilon\tilde{\mathbf{A}}^{(0)}$, where $\tilde{\mathbf{A}}^{(0)} = \mathbf{A}^{(1)}\mathbf{A}^{(0)}$. According to $\tilde{\mathbf{F}}^{(0)} = \mathbf{F}^{(1)}\mathbf{F}^{(0)} = \mathbf{F}^{(1)}\mathbf{A}^{(0)}\mathbf{GS}$ and $\tilde{\mathbf{F}}^{(0)} = \tilde{\mathbf{A}}^{(0)}\mathbf{GS}$, the incremental deformation for $\tilde{\mathbf{A}}^{(0)}$ is

$$\tilde{\mathbf{A}}^{(0)} = \mathbf{F}^{(1)}\mathbf{A}^{(0)}, \tag{18}$$

by which we have $\tilde{\mathbf{A}} = \tilde{\mathbf{A}}_{\mathrm{I}}\mathbf{A}^{(0)}$ and $\mathbf{F}^{(1)} = \mathbf{A}^{(1)}$, where $\tilde{\mathbf{A}}_{\mathrm{I}} = \mathbf{I} + \varepsilon\mathbf{F}^{(1)}$. Additionally, because of the instantaneity of $\mathbf{F}^{(1)}$ and incompressibility for $\tilde{\mathbf{A}}$ and $\mathbf{A}^{(0)}$, we obtain $\det(\tilde{\mathbf{A}}_{\mathrm{I}}) = \det(\mathbf{I}) + \varepsilon\operatorname{tr}(\mathbf{F}^{(1)}) = 1$ to first order.

Next, the superimposed incremental incompressibility condition is

$$\operatorname{tr}(\mathbf{F}^{(1)}) = 0. \tag{19}$$

Because $\mathbf{F}^{(1)}$ is expressed in B_c, by extending the constitutive rules, which results in the linearized constitutive equations, we can further connect the stress tensor to the deformation gradient. For the incompressible case, the smooth scalar function $C^{(0)}$ satisfies the equations $\partial C^{(0)}/\partial \mathbf{A}^{(0)} = (\det(\mathbf{A}^{(0)}))(\mathbf{A}^{(0)})^{-1}$ and $C\mathbf{F}^{(1)} = -\mathbf{F}^{(1)}$. Therefore, we have

$$\mathbf{T}^{(0)} = \mathbf{A}^{(0)}\frac{\partial \Psi^{(0)}}{\partial \mathbf{A}^{(0)}} - q^{(0)}\mathbf{I} \quad \text{and} \quad \mathbf{T}^{(1)} = \mathcal{L}\mathbf{F}^{(1)} + \mathbf{F}^{(1)}\mathbf{A}^{(0)}\frac{\partial \Psi^{(0)}}{\partial \mathbf{A}^{(0)}} - q^{(1)}\mathbf{I}, \tag{20}$$

and the incremental first Piola–Kirchhoff stress tensor in B_c is

$$\mathbf{P}_0^{(1)} = \mathcal{L}\mathbf{F}^{(1)} + q^{(0)}\mathbf{F}^{(1)} - q^{(1)}\mathbf{I}, \tag{21}$$

where $\mathcal{L}$ represents the instantaneous elastic modulus, and the only nonzero components of this fourth-order tensor are provided in Supplementary. Then, the incremental equilibrium equation (i.e., $\operatorname{div}(\mathbf{T}^{(1)}) = 0$ or $\operatorname{div}(\mathbf{P}_0^{(1)}) = 0$) can be rewritten in a unified form

$$\operatorname{div}(\mathcal{L}\mathbf{F}^{(1)}) + (\mathbf{F}^{(1)})^{\mathrm{T}}\operatorname{grad}(q^{(0)}) - \operatorname{grad}(q^{(1)}) = \mathbf{0}. \tag{22}$$

4.2. Incremental field, stroh formulation, and surface impedance method

The general incremental displacement vector $\mathbf{u} = \chi^{(1)}(\mathbf{x})$ can be given as

$$\chi^{(1)} = [u(r, \theta, z), v(r, \theta, z), w(r, \theta, z)], \tag{23}$$

where (r, θ, z) are curvilinear coordinates. In particular, for axisymmetric deformation, $\mathbf{u}$ is independent of z. Moreover, the incremental displacement gradient tensor $\mathbf{F}^{(1)}$ takes the form

$$\mathbf{F}^{(1)} = \begin{bmatrix} \frac{\partial u}{\partial r} & r^{-1}\left(\frac{\partial u}{\partial \theta} - v\right) & \frac{\partial u}{\partial z} \\ \frac{\partial v}{\partial r} & r^{-1}\left(\frac{\partial v}{\partial \theta} + u\right) & \frac{\partial v}{\partial z} \\ \frac{\partial w}{\partial r} & r^{-1}\frac{\partial w}{\partial \theta} & \frac{\partial w}{\partial z} \end{bmatrix}, \tag{24}$$

and then the incremental incompressibility condition requires

$$\frac{\partial u}{\partial r} + r^{-1}(\frac{\partial v}{\partial \theta} + u) + \frac{\partial w}{\partial z} = 0, \tag{25}$$

based on which we look for a nontrivial solution by assuming the following ansatz:

$$[u, \mathrm{P}_{0rr}^{(1)}, q^{(1)}] = [\mathcal{U}(r), \mathcal{P}_{rr}(r), \mathcal{Q}(r)]\cos(m\theta)\cos(kz),$$
$$[v, \mathrm{P}_{0r\theta}^{(1)}] = [\mathcal{V}(r), \mathcal{P}_{r\theta}(r)]\sin(m\theta)\cos(kz), \quad \text{and} \quad [w, \mathrm{P}_{0rz}^{(1)}] = [\mathcal{W}(r), \mathcal{P}_{rz}(r)]\cos(m\theta)\sin(kz), \tag{26}$$

where the integer m is the hoop wavenumber, $k = n\pi/(\lambda_3 L)$ is the axial half wavenumber (n is an integer), and $\mathcal{U}$, $\mathcal{V}$, $\mathcal{W}$, $\mathcal{P}_{ij}$, and $\mathcal{Q}$ are scalar functions of r only.

The Stroh formalism with the optimal Hamiltonian form can be created for the bifurcation analysis problem. Therefore, we can convert the set of partial differential equations into a set of ordinary differential equations. To express the incremental equilibrium

equations and incompressibility conditions in a refined form (Destrade et al., 2009; Du et al., 2020), we introduce the incremental displacement–traction vector $\boldsymbol{\eta}(r)$ as

$$\boldsymbol{\eta}(r) = [\mathbb{U}(r), r\mathbb{S}(r)]^{\mathrm{T}}, \quad \mathbb{U}(r) = [\mathcal{U}(r), \mathcal{V}(r), \mathcal{W}(r)]^{\mathrm{T}}, \text{ and } \mathbb{S}(r) = \left[\mathcal{P}_{rr}(r), \mathcal{P}_{r\theta}(r), \mathcal{P}_{rz}(r)\right]^{\mathrm{T}}, \tag{27}$$

where $\mathbb{U}(r)$ and $\mathbb{S}(r)$ are the displacement and traction vectors, respectively.

It transpires that previous work on the Stroh formulation is applicable only to neo-Hookean materials. Here, we provide the expanded formulation for hyperelastic materials with strain-stiffening effects based on the symmetry of the strain energy density. With these basic assumptions, the incremental problem can be rewritten as

$$\frac{d\boldsymbol{\eta}(r)}{dr} = r^{-1}\boldsymbol{G}(r)\boldsymbol{\eta}(r) = r^{-1}\begin{bmatrix} \boldsymbol{G}_1(r) & \boldsymbol{G}_2(r) \\ \boldsymbol{G}_3(r) & \boldsymbol{G}_4(r) \end{bmatrix}\boldsymbol{\eta}(r), \tag{28}$$

where $\boldsymbol{G}(r)$ is the Stroh matrix, and its components (the 3×3 sub-blocks) can be calculated as

$$\boldsymbol{G}_1(r) = \begin{bmatrix} -1 & -m & -kr \\ \frac{m(\mathcal{L}_{r\theta\theta r}+q^{(0)})}{\mathcal{L}_{r\theta r\theta}} & \frac{\mathcal{L}_{r\theta\theta r}+q^{(0)}}{\mathcal{L}_{r\theta r\theta}} & 0 \\ \frac{kr(\mathcal{L}_{rzzr}+q^{(0)})}{\mathcal{L}_{rzrz}} & 0 & 0 \end{bmatrix}, \quad \boldsymbol{G}_2(r) = \begin{bmatrix} 0 & 0 & 0 \\ 0 & \mathcal{L}_{r\theta r\theta}^{-1} & 0 \\ 0 & 0 & \mathcal{L}_{rzrz}^{-1} \end{bmatrix}, \quad \boldsymbol{G}_3(r) = \begin{bmatrix} \mathcal{K}_{11} & \mathcal{K}_{12} & \mathcal{K}_{13} \\ \mathcal{K}_{21} & \mathcal{K}_{22} & \mathcal{K}_{23} \\ \mathcal{K}_{31} & \mathcal{K}_{32} & \mathcal{K}_{33} \end{bmatrix}, \tag{29}$$

with $\boldsymbol{G}_4(r) = \bar{\boldsymbol{G}}_1^{\mathrm{T}}(r)$ and the explicit forms regarding $\mathcal{K}_{11}$–$\mathcal{K}_{33}$ given in Supplementary.

To describe the strain-stiffening effect of Gent materials, the modulus $\mathcal{L}_{jikl}$ can be calculated as

$$\mathcal{L}_{jikl} = \frac{\mu}{\mathcal{J}_m - \mathbf{C}_a : \mathbf{I} + 3}\left(\delta_{il}(\mathbf{B}_a)_{jk} + \frac{2(\mathbf{B}_a)_{ij}(\mathbf{B}_a)_{kl}}{\mathcal{J}_m - \mathbf{C}_a : \mathbf{I} + 3}\right), \tag{30}$$

where δ_{il} is the Kronecker delta, and $\mathbf{C}_a$ and $\mathbf{B}_a$ are the right and left Cauchy–Green tensors, respectively. As the level of strain stiffening tends to infinity, the modulus $\mathcal{L}_{jikl}$ converges to the form of the neo-Hookean model (i.e., $\mathcal{L}_{jikl} = \mu\delta_{il}(\mathbf{B}_a)_{jk}$). In other words, the neo-Hookean model is a limiting case of the more general model that accounts for strain stiffening.

Because of the variable coefficient in $\boldsymbol{G}(r)$, the incremental issue involving hyperelastic tubes cannot be solved analytically. Instead, the surface impedance matrix technique is a self-contained, effective, and reliable computational approach for investigating bifurcation issues in inhomogeneous materials.

We introduce the conditional impedance matrix $\mathcal{Z}^i(r, r_i)$ such that

$$r\mathbb{S}(r) = \mathcal{Z}^i(r, r_i)\mathbb{U}(r), \tag{31}$$

where $\mathcal{Z}^i(r, r_i)$ depends on an auxiliary condition at $r = r_i$. Next, we focus on the procedure for constructing matrix $\mathcal{Z}^i(r, r_i)$. Plugging the impedance matrix into the incremental equilibrium equations, we obtain

$$\frac{d\mathbb{U}}{dr} = r^{-1}(\boldsymbol{G}_1\mathbb{U} + \boldsymbol{G}_2\mathcal{Z}^i\mathbb{U}) \text{ and } \frac{d\mathcal{Z}^i}{dr}\mathbb{U} + \mathcal{Z}^i\frac{d\mathbb{U}}{dr} = r^{-1}(\boldsymbol{G}_3\mathbb{U} + \bar{\boldsymbol{G}}_1^{\mathrm{T}}\mathcal{Z}^i\mathbb{U}), \tag{32}$$

and then eliminating the displacement vector gives a Riccati differential equation:

$$\frac{d\mathcal{Z}^i}{dr} = r^{-1}(\boldsymbol{G}_3 + \boldsymbol{G}_4\mathcal{Z}^i - \mathcal{Z}^i\boldsymbol{G}_1 - \mathcal{Z}^i\boldsymbol{G}_2\mathcal{Z}^i). \tag{33}$$

From Eq. (33), nontrivial solutions and the critical growth-induced instability states exist whenever the matrix $\mathcal{Z}^i(r, r_i)$ satisfies

$$\det(\mathcal{Z}^i(r_o, r_i)) = 0. \tag{34}$$

Once the convergence criterion in Eq. (34) is reached, we can obtain the incremental displacement field of the cylindrical tube by integrating Eq. $(32)_1$ and $\mathcal{Z}^i(r_o, r_i)\mathbb{U}(r_o) = \mathbf{0}$.

5. Results for growth instability with strain-stiffening effect

5.1. Differential growth evolution

The perturbation technique described in Section 4 provides a precise means of solving the equilibrium problem [i.e., Eq. (2)] in the proximity of the critical point. In this section, we investigate how a range of synergistic factors – including initial residual stress, thickness, axial stretch ratio, internal pressure, growth rate, and the strain-stiffening effect – can significantly affect the initiation of growth instability and the resulting remodeling pattern morphology. Importantly, we find that for biological tissues in which strain stiffening occurs at higher strain (such as $\mathcal{J}_m > 21$), the maximum critical growth ratio tends to be consistent with the calculated results of the neo-Hookean model. When strain stiffening occurs in biological tissues under moderate strain (such as $0.46 < \mathcal{J}_m < 21$), the strain-stiffening effect leads to a significant retardation in the growth instability of the system compared to the neo-Hookean model. Lastly, when tissues are stiffened at very small strain (such as $\mathcal{J}_m < 0.46$), the occurrence of growth instability is prevented, resulting in the retention of a smooth hyperelastic cylindrical tube configuration.

In most vertebrates, tissue growth and remodeling undergo a sequence of differentiation processes that ultimately result in the development of functionalized structures with either unidirectional or intricate fold networks. The differentiation process involves
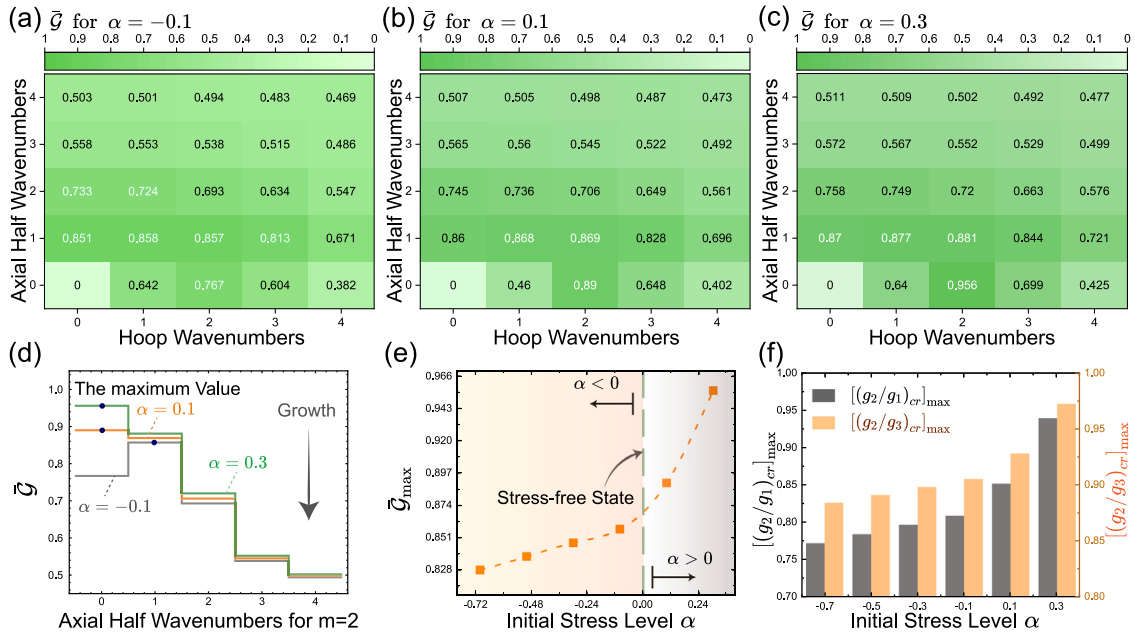
Fig. 6. Existence of maximum critical growth ratio $\bar{\mathcal{G}}_{\max}$ for different wrinkle wavenumbers m and n when initial stress level α is (a) -0.1, (b) 0.1, and (c) 0.3. (d) Critical differential growth ratio $\bar{\mathcal{G}}$ as a step function of wavenumber n for hoop wavenumber $m = 2$, illustrating the existence of maximum critical growth ratio and growth direction. (e) Maximum critical growth ratio $\bar{\mathcal{G}}_{\max}$ as a function of initial stress level α; note that $\alpha = 0$ represents the initially stress-free state. (f) Evolutions of $[(g_2/g_1)_{cr}]_{\max}$ and $[(g_2/g_3)_{cr}]_{\max}$ for different initial residual stress level α.

the interplay of growth factors and compressive stresses that accumulate in the direction of rapid growth. When the stress threshold is exceeded, tissue growth and remodeling become unstable. This process underscores the strong link between smooth muscle differentiation and the differential growth nature of tissue morphogenesis. Drawing from the aforementioned considerations, it is posited that the evolution (Eskandari and Kuhl, 2015) of the growth-deformation gradient tensor can be represented by $g_i(t) = 1 + \dot{\mathcal{G}}_i t$ for $i = 1, 2, 3$, where $\dot{\mathcal{G}}_i$ represent the constant growth rates (the linear form of growth kinematics). To further characterize the differential growth process, we establish the following relationships:

$$\dot{G}_v = \dot{\mathcal{G}}_2 / \dot{\mathcal{G}}_1 = (g_2 - 1)/(g_1 - 1) \text{ and } \dot{G}_w = \dot{\mathcal{G}}_2 / \dot{\mathcal{G}}_3 = (g_2 - 1)/(g_3 - 1). \tag{35}$$

In this scenario (for the specific strain stiffening level), if g_2 is regarded as a conditional parameter, then the remaining two growth factors g_1 and g_3 can be represented respectively by $\dot{G}_v$ and $\dot{G}_w$, i.e., $g_1(t) = \dot{G}_v^{-1}(g_2(t) - 1) + 1$ and $g_3(t) = \dot{G}_w^{-1}(g_2(t) - 1) + 1$. Without loss of generality, given a growth factor ordering of $g_1(t) > g_3(t) > g_2(t)$ and a strain stiffening level $\mathcal{J}_m$ during growth in biological tissues (Shyer et al., 2013; Ben Amar and Jia, 2013), we can select $\dot{G}_v = 0.1$ and $\dot{G}_w = 0.2$ as simulation parameters to fulfill the modeling requirements.

Our computational approach involves identifying the critical differential growth ratios $(g_2/g_1)_{cr}, (g_2/g_3)_{cr}$ and their average value $\bar{\mathcal{G}} = ((g_2/g_1)_{cr} + (g_2/g_3)_{cr})/2$, thereby permitting incremental solutions for given wrinkle wavenumbers. We evaluate all possible wrinkle numbers in the hoop and axial directions and select the largest ratio to determine the onset of growth instability. Specifically, to underscore the importance of this physical quantity (i.e., the maximum ratio to trigger growth instability), we propose the notion of a maximum critical growth ratio $\bar{\mathcal{G}}_{\max}$, i.e.,

$$\bar{\mathcal{G}}_{\max} = \max[\bar{\mathcal{G}}] = \frac{1}{2}[(g_2/g_1)_{cr}]_{\max} + \frac{1}{2}[(g_2/g_3)_{cr}]_{\max}. \tag{36}$$

If both critical wavenumbers m_{cr} and n_{cr} are nonzero, then the system exhibits three-dimensional coupling growth instability. Note that m_{cr} and n_{cr} cannot be zero simultaneously.

5.2. Strain stiffening and retardation instability

Fig. 6 illustrates the existence of a maximum critical growth ratio $\bar{\mathcal{G}}_{\max}$ for each initially residually stressed state. The initial stress level α plays a significant role in modulating the growth instability of biological tissues. Notably, the strain-stiffening level is finite ($\mathcal{J}_m = 10$), suggesting that the instability of growth is influenced by synergistic factors. Fig. 6(a) reveals that the biological tissue with residual stress undergoes growth instability when $\alpha = -0.1$, provided that the maximum critical growth ratio is 0.858 and the circumferential and axial critical instability wavenumbers are both 1 [i.e., $(m_{cr}, n_{cr}) = (1, 1)$]. For $\alpha = 0.1$ [see Fig. 6(b)] and $\alpha = 0.3$ [see Fig. 6(c)], the maximum critical growth ratios are 0.869 and 0.956, respectively, with the instability wavenumbers

being $(2, 1)$ and $(2, 0)$. For wavenumber $m = 2$, Fig. 6(d) shows the stepped curves depicting the evolution of the critical differential growth ratio $\bar{\mathcal{G}}$, providing evidence for the presence of a maximum critical growth ratio $\bar{\mathcal{G}}_{\max}$; the arrow in the figure represents the growth direction of the biological tissue. Fig. 6(e) shows the nonlinear evolution pattern of the maximum critical growth ratio for various initial residual stress levels; the maximum critical growth ratio increases nonlinearly with linearly increasing initial stress level. Note that $\bar{\mathcal{G}}_{\max}$ exhibits a more pronounced increase for higher initial residual stress level (such as $\alpha > 0$), as demonstrated in Fig. 6(e). At $\alpha = 0$, the biological tissue is in a state of free initial residual stress [see the vertical dashed line in Fig. 6(e)]. Moreover, as shown in Fig. 6(f), $[(g_2/g_1)_{cr}]_{\max}$ and $[(g_2/g_3)_{cr}]_{\max}$ exhibit a similar growth pattern to that of $\bar{\mathcal{G}}_{\max}$ with increasing initial residual stress level [as observed in Fig. 6(e)]. To avoid additional complications, in this research we focus on the effects of strain stiffening on the maximum critical growth ratio $\bar{\mathcal{G}}_{\max}$.

As noted previously, the parameter $\mathcal{J}_m$ serves as an indicator of the level of strain stiffening in a material model. As $\mathcal{J}_m$ decreases, a smaller applied strain can cause a steeper increase in the stress–strain curve of the biomaterial, while larger $\mathcal{J}_m$ implies a "softer" material property. As $\mathcal{J}_m$ tends to positive infinity, the strain-stiffened material degenerates to the neo-Hookean model.

Fig. 7 shows the relationship between the maximum critical growth ratio $\bar{\mathcal{G}}_{\max}$ and different levels of strain stiffening for a specific initial residual stress level ($\alpha = -0.5$). As shown in Fig. 7(a)–(f), each level of strain stiffening corresponds to a specific maximum critical growth ratio that triggers growth instability in biological tissues. More precisely, the values of the maximum critical growth ratio $\bar{\mathcal{G}}_{\max}$ for $\mathcal{J}_m = 5, 10, 15, 20, 25$, and 30 are 0.836, 0.838, 0.839, 0.84, 0.841, and 0.841, respectively. Equally, Fig. 7(a)–(f) depict the nonlinear step diagrams of the critical differential growth ratio for each case, corresponding to circumferential and axial instability wave numbers of 1; these diagrams were constructed using a similar approach for all cases. Additionally, Fig. 7(g) shows a noteworthy phenomenon that emerges upon summarizing and extending the range of strain-stiffening levels: the manifestation of retarded instability resulting from the strain-stiffening effect. More specifically, when strain stiffening occurs in biological tissues at higher strain (i.e., $\mathcal{J}_m > 21$), the maximum critical growth ratio $\bar{\mathcal{G}}_{\max}$ remains the same as that calculated using the neo-Hookean model/material. When biological tissues undergo moderate strain and experience strain stiffening (i.e., $0.46 < \mathcal{J}_m < 21$), the curve of maximum critical growth ratio tends to shift downward continuously [see Fig. 7(g) for details]. This observation suggests that the strain-stiffening effect causes a substantial delay in growth instability compared to the predictions of the neo-Hookean model. In contrast, for $0 < \mathcal{J}_m < 0.46$, the strain-stiffening effect prevents growth instability and maintains a smooth hyperelastic cylindrical tube configuration; this indicates that instability morphology will never form and that the epithelial tissue remains smooth for all levels of growth. These events resulting from the strain-stiffening effects provide significant evidence for the retardation instability of soft matter in both an individual surface crease (Jin and Suo, 2015) and the fingering or fringe instability (Lin et al., 2018). To illustrate further the delayed instability phenomenon resulting from strain stiffening, we undertake a detailed analysis of the geometric and stress-related evolution, presented in Fig. 7(h). As shown, for strain-stiffening levels greater than 21 ($\mathcal{J}_m > 21$), both the maximum critical radius ratio $[(r_o/r_i)_{cr}]_{\max}$ and the maximum critical Cauchy stress ratio $[(T_{rr}|_{r=r_o}/T_{rr}|_{r=r_i})_{cr}]_{\max}$ approach the corresponding values obtained from the neo-Hookean model, which are indicated by $\mathcal{J}_m$ tending to infinity. In the range of $0.46 < \mathcal{J}_m < 21$, the values of the maximum critical radius ratio and Cauchy stress exceed the corresponding values for $\mathcal{J}_m \to \infty$. When $\mathcal{J}_m$ is below 0.46, growth instability ceases to occur. Fig. 7(i) shows the maximum critical volume variation, denoted by $[(\det \mathbf{G})_{cr}]_{\max}$, for the biological tissue. As the strain-stiffening level increases, the material properties become softer, resulting in smaller values of $[(\det \mathbf{G})_{cr}]_{\max}$, which eventually converge to those of the neo-Hookean material.

Strain stiffening significantly retards the growth instability of biological tissues, and a key challenge is to understand how the level of strain stiffening affects the morphological selection of such tissues. Within the regime of retardation instability (such as $5 < \mathcal{J}_m < 25$), we generated a parameter space of maximum critical growth ratio $\bar{\mathcal{G}}_{\max}$ by calculating 3125 values for $\alpha, \mathcal{J}_m$, and R_o/R_i (denoted as $[\alpha, \mathcal{J}_m, R_o/R_i]$), as shown in Fig. 8(a). First, we perform a horizontal dissection of this three-dimensional distribution by using a planar cut parameter space with $R_o/R_i = 1.1, 1.2$, and 1.3, as illustrated in Fig. 8(b)–(d), respectively. In Fig. 8(b), we observe that a higher level of strain stiffening $\mathcal{J}_m$ and a larger value of α result in a higher maximum critical growth ratio $\bar{\mathcal{G}}_{\max}$, which leads to a transition in the morphological selection of this biological tissue from type-I coupled growth instability to type-II hoop growth instability. For slightly larger initial radius ratio, as depicted in Fig. 8(c), the strain-stiffening effect becomes dominant in pattern selection. A higher level of strain stiffening, indicating softer material properties, is capable of inducing a transition in morphological selection from type I to type II. When the initial radius ratio is larger [see Fig. 8(d) for details], the transformation of morphological selection from type-III axial growth instability to type-II coupled growth instability is controlled by the level of strain stiffening. Naturally, larger $\mathcal{J}_m$ corresponds to larger maximum critical growth ratio $\bar{\mathcal{G}}_{\max}$.

Knowing the critical instability wavenumbers (m_{cr}, n_{cr}) and the maximum critical growth ratio $\bar{\mathcal{G}}_{\max}$, we can calculate the mechanical displacement field for hyperelastic strain-stiffening cylindrical tube growth. Fig. 8(e) shows the instability morphology for various levels of strain stiffening in response to the specific cases of $[\alpha, \mathcal{J}_m, R_o/R_i]$ shown in Fig. 8(b)–(d). Types I, II, and III correspond to coupled, hoop, and axial growth instability, respectively.

The parameter space in Fig. 8(a) shows that strain stiffening and initial radius ratio have a synergistic effect on growth instability (the maximum critical growth ratio $\bar{\mathcal{G}}_{\max}$). For a fixed value of α [e.g., $\alpha = 0.1$ as illustrated in Fig. 9(a)], a larger initial radius ratio R_o/R_i for a smaller level of strain stiffening yield a smaller $\bar{\mathcal{G}}_{\max}$. As $\mathcal{J}_m$ increases, the evolution of the maximum critical growth ratio $\bar{\mathcal{G}}_{\max}$ shifts gradually from a monotonically decreasing curve to a nonmonotonic one and eventually to a slightly monotonic increase (e.g., the curve corresponding to $\mathcal{J}_m = 25$). This is supported further by slicing the three-dimensional distribution in Fig. 8(a) along the two vertical planes of $\alpha = 0$ and $\alpha = -0.1$, as shown in Figs. 9(b) and (c). With lower strain stiffening and larger initial radius ratio, the resulting maximum critical growth ratio is smaller, indicating a greater difficulty for growth instability to occur in biological tissues. Moreover, as shown in Fig. 9(d), we observe that for certain levels of strain stiffening and initial residual stress (e.g., $\mathcal{J}_m = 5$ and $\alpha = 0.1$), smaller initial radius ratio results in instability morphologies that are more intricate and elegant, thereby
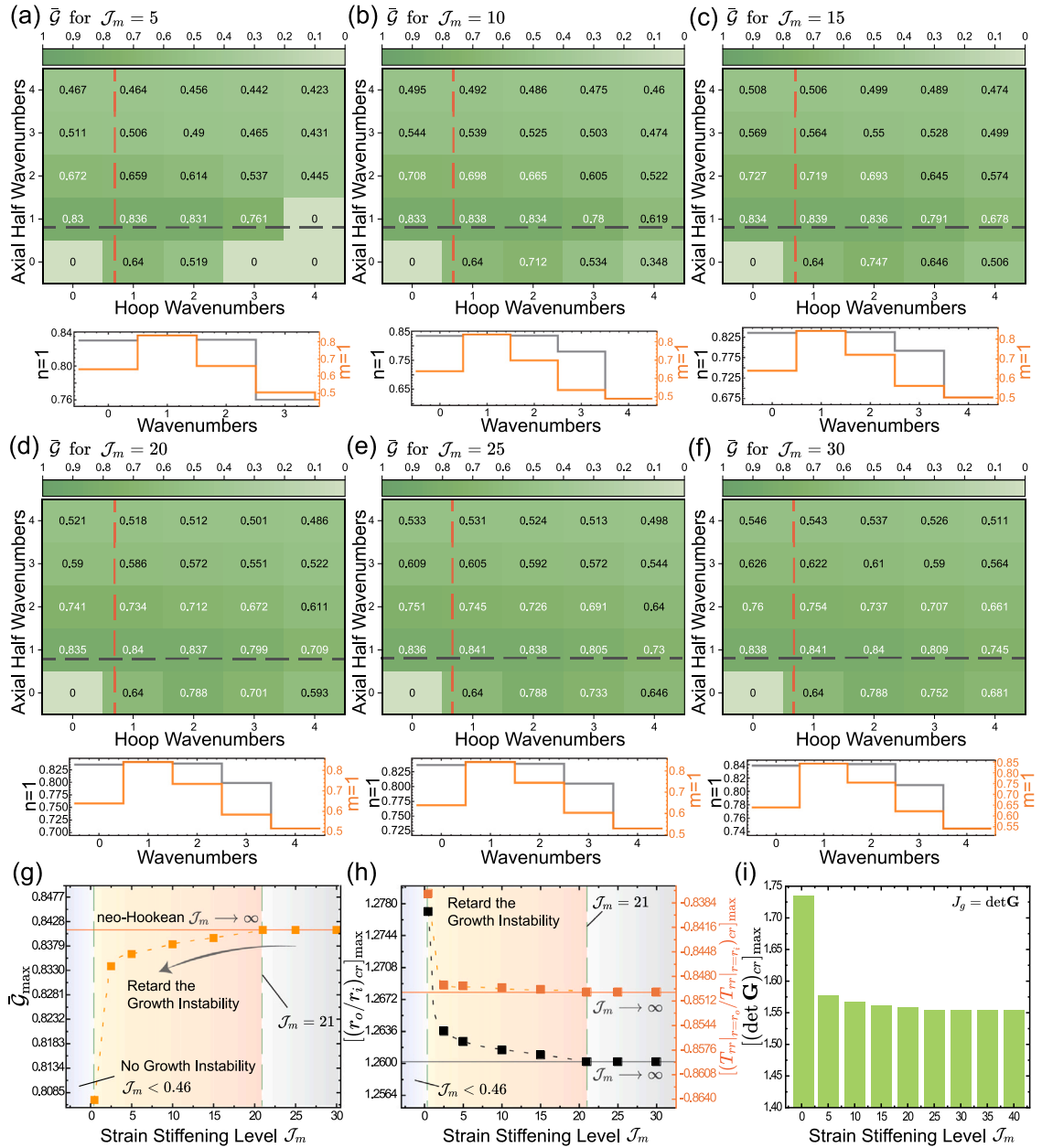
Fig. 7. Existence of maximum critical growth ratio $\bar{\mathcal{G}}_{\max}$ for different wrinkle wavenumbers m and n when the strain-stiffening level $\mathcal{J}_m$ is (a) 5, (b) 10, (c) 15, (d) 20, (e) 25, and (f) 30. (g) Maximum critical growth ratio $\bar{\mathcal{G}}_{\max}$ as a function of strain-stiffening level $\mathcal{J}_m$. For $\mathcal{J}_m > 21$, the maximum critical growth ratio $\bar{\mathcal{G}}_{\max}$ remains the same as that predicted by the neo-Hookean model. For $0.46 < \mathcal{J}_m < 21$, the curve of maximum critical growth ratio shifts downward, causing a delay in growth instability compared to the neo-Hookean model. However, for $0 < \mathcal{J}_m < 0.46$, the strain-stiffening effect prevents growth instability. (h) Maximum critical radius ratio $[(r_o/r_i)_{cr}]_{\max}$ and Cauchy stress ratio $[(T_{rr}|_{r=r_o}/T_{rr}|_{r=r_i})_{cr}]_{\max}$ as functions of strain-stiffening level $\mathcal{J}_m$. (i) Evolution of maximum critical volume variation $[(\det \mathbf{G})_{cr}]_{\max}$ for different strain-stiffening levels.

broadening the selection space of the model for this biological tissue. As the initial radius ratio increases, both the critical hoop wavenumber m_{cr} and the critical axial wavenumber n_{cr} decrease continuously.

The most significant physical implication of growth instability with strain-stiffening effects is its complex modulation by multiple factors. Fig. 10 demonstrates the multifactorial control of growth instability by axial tensile ratio λ_3, internal pressure Q, and growth rate $\dot{G}_v$ at specific levels of strain stiffening. In Fig. 10(a), we observe that for different values of λ_3, the curves of maximum critical growth ratio $\bar{\mathcal{G}}_{\max}$ diverge initially and then converge to a single curve as the level of strain stiffening increases, with the convergence occurring at $\mathcal{J}_m = 10$. To investigate further the effect of λ_3 on the maximum critical growth ratio at $\mathcal{J}_m = 5$, Fig. 10(b) shows the nonlinear evolution of $\bar{\mathcal{G}}_{\max}$ from the tension region to the compression region of the biological tissue. As λ_3 decreases, the maximum
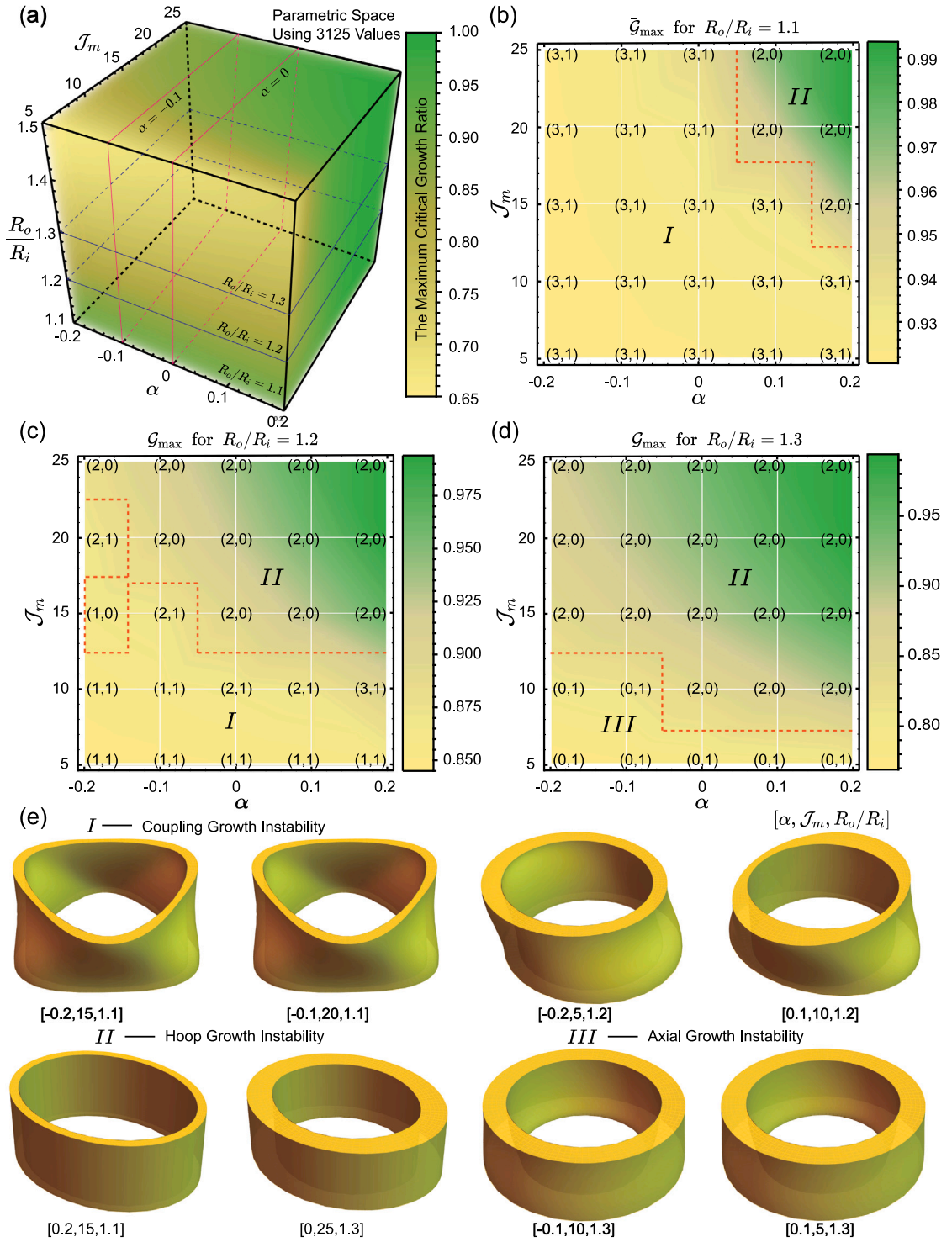
Fig. 8. (a) Parameter space of maximum critical growth ratio $\bar{\mathcal{G}}_{\max}$ obtained by calculating 3125 values for $\mathcal{J}_m$, R_o/R_i, and α. Distribution of maximum critical growth ratio for different $\mathcal{J}_m$ and α when $R_o/R_i =$ (b) 1.1, (c) 1.2, and (d) 1.3. (e) Instability morphologies under different levels of strain stiffening for specific cases of $\left[\alpha, \mathcal{J}_m, R_o/R_i\right]$. The observed growth instabilities are categorized into three types: type I corresponds to coupled growth instability, type II corresponds to hoop growth instability, and type III corresponds to axial growth instability.
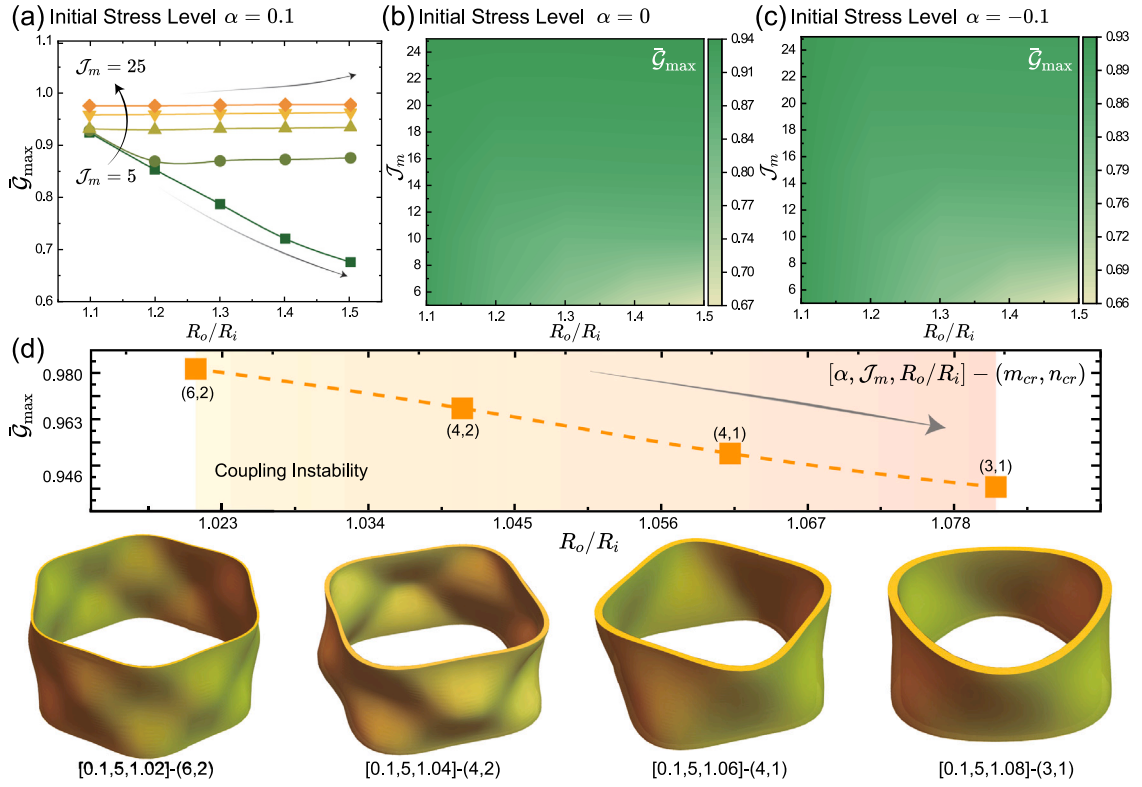
Fig. 9. (a) Evolution of maximum critical growth ratio $\bar{\mathcal{G}}_{max}$ for different strain-stiffening levels and initial radius ratio when $\alpha = 0.1$. Distribution of maximum critical growth ratio for different $\mathcal{J}_m$ and R_o/R_i when $\alpha =$ (b) 0 and (c) −0.1. (d) Instability morphologies under different levels of strain stiffening for specific cases of $[\alpha, \mathcal{J}_m, R_o/R_i]$. Note that when the initial radius ratio is smaller, the resulting instability morphology is more intricate and elegant. This expands the selection space of the model for biological tissues.
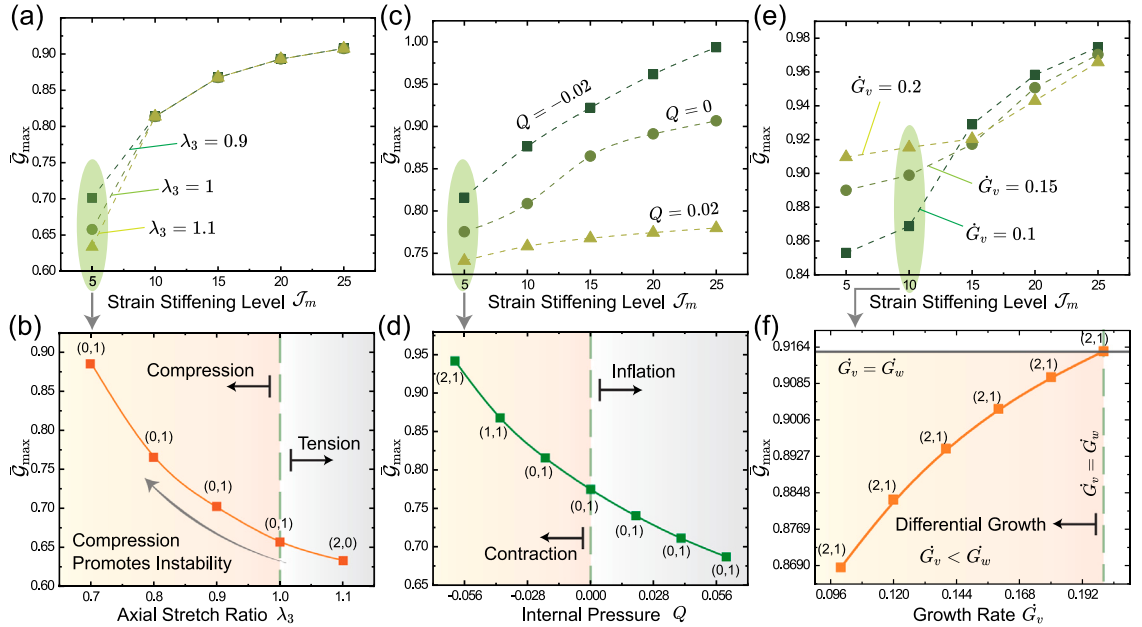

Fig. 10. Controlling growth instability through multifactorial manipulation of axial tensile ratio λ_3, internal pressure Q, and growth rate $\dot{G}_v$ under defined levels of strain stiffening. (a) Evolution of maximum critical growth ratio $\bar{\mathcal{G}}_{max}$ for different strain-stiffening levels and λ_3. (b) Maximum critical growth ratio as a function of axial tensile ratio when $\mathcal{J}_m = 5$. (c) Evolution of maximum critical growth ratio $\bar{\mathcal{G}}_{max}$ for different strain-stiffening levels and Q. (d) Maximum critical growth ratio as a function of pressure when $\mathcal{J}_m = 5$. (e) Evolution of maximum critical growth ratio $\bar{\mathcal{G}}_{max}$ for different strain-stiffening levels and $\dot{G}_v$. (f) Maximum critical growth ratio as a function of growth rate $\dot{G}_v$ when $\mathcal{J}_m = 10$.

critical growth ratio $\bar{\mathcal{G}}_{\max}$ increases. Fig. 10(c) shows that $\bar{\mathcal{G}}_{\max}$ increases monotonically as the level of strain stiffening increases under various values of the internal pressure. When larger Q is present from the contracted region to the inflation region of the biological tissue, smaller $\bar{\mathcal{G}}_{\max}$ is observed for given $\mathcal{J}_m$ [see Fig. 10(d)]. Fig. 10(e) and (f) explore how the growth rate $\dot{G}_v$ affects the growth instability. As shown, the maximum critical growth ratio $\bar{\mathcal{G}}_{\max}$ tends to increase with higher levels of strain stiffening, indicating that biological tissues are more susceptible to growth instability. On the other hand, for a specific $\mathcal{J}_m$ value (e.g., $\mathcal{J}_m = 10$), the maximum critical growth ratio increases continuously with increasing $\dot{G}_v$. However, when $\mathcal{J}_m$ is greater than 15, the trend in the evolution of $\bar{\mathcal{G}}_{\max}$ is completely reversed. Overall, this study delves deeper into the impact of strain stiffening, inhomogeneous growth, and initial residual stress on tissue growth and airway remodeling through a well-supported model. The findings reveal the significance of delayed growth instability and its consequences for clinical interventions. Although the model simplifies the complexity of tissue properties and boundary conditions, it provides a valuable basis for future research on more advanced models, anisotropic features, and multiscale mechanisms.

6. Discussion and conclusions

Airway remodeling is the term used to describe structural changes that occur in individuals with chronic inflammatory airway disorders such as asthma, chronic obstructive pulmonary disease, bronchiectasis, and cystic fibrosis (Hirota and Martin, 2013). These changes begin with an initial residual stress state and cause a strain-stiffening effect due to increased and tightened collagen, leading to tissue nonlinearity and mucosal folding (Hough et al., 2020). In asthmatic patients, persistent remodeling has been associated with airway hyperresponsiveness (Black et al., 2001; Tagaya and Tamaoki, 2007), which causes symptoms such as coughing, chest tightness, and dyspnea. Unfortunately, no known medications can reverse airway remodeling, and there are no accurate noninvasive methods for quantifying it.

Motivated by experimental studies on strain stiffening in growth and remodeling, herein we presented a robust framework that describes the effects of strain stiffening on mass reorganization in residually stressed biological tissues. In this work, we characterized biological growth as a triphasic decomposition of the overall deformation gradient that begins with an initial stress ground state and subsequently incorporates strain-stiffening effects into various aspects of growth deformation. Our theory provides a comprehensive description of the free energy density and Cauchy stress of tissue growth, accounting for both initial stress and strain-stiffening effects. This framework enables the systematic analysis of differential growth and nonlinear symmetry morphology in biological tissues. Through perturbation analysis, we conducted an in-depth exploration of the effects of strain stiffening on morphological selection in biological tissues, resulting in the discovery of significant retardation in instability induced by strain stiffening and initial residual stress. To provide demonstrative clarification, we selected a clinically motivated example of biological growth, i.e., the changes in tissue, cellular, and molecular composition associated with airway remodeling. Notwithstanding the diverse microstructural features of volume alterations, we used nonlinear field theory to uncover the instability characteristics of growth, mechanical instability scenarios, and morphological bifurcation with delayed onset that result from strain stiffening.

To clarify, we began by discussing the contrasts and similarities between the Kröner–Lee and triphasic decompositions. The triphasic decomposition involves creating two distinct stress-free virtual configurations that contain incompatible and discrete tissue states. In contrast, the Kröner–Lee decomposition is a method for separating the deformation of a material into elasticity and growth components. We developed equations for the Cauchy stress and the first Piola–Kirchhoff stress using the commutativity of the deformation gradient tensor, and we determined formulae for the initial residual stress and initial elastic deformation.

Next, we proceeded to apply the Gent model, which enabled us to develop a free energy density function and constitutive equations for nonlinear strain-stiffening biomaterials that exhibit initial residual stress. The Lagrangian multiplier and strain stiffening parameters satisfy a cubic equation, in accordance with the assumption of isochoric deformation. To derive the three-dimensional initial stress state, we introduced a stress potential function in logarithmic form. We subsequently determined the growth stress field and established the integral equation that satisfies the Cauchy stress. We then conducted a systematic discussion of the results obtained for the ground state, taking into account factors such as differential growth, initial residual stresses, and the effects of strain stiffening.

Subsequently, we investigated the remodeling and morphological bifurcation behavior of tubes with strain-stiffening and initial-residual-stress effects using perturbation theory. By introducing first-order kinematic relations, we obtained superimposed incremental incompressibility conditions and incremental equilibrium equations. The corresponding bifurcation problem was transformed into the Stroh formulation by formulating the incremental displacement field. We then used the surface impedance method to evaluate the overall incremental displacement and incremental traction fields.

By growth instability analysis, we found that a maximum differential growth ratio exists for each initial configuration, initial residual stress state, strain stiffening level, and initial radius ratio. The extent of strain stiffening has a crucial role in the regulation of growth instability, and it can effectively impede the growth instability of biological tissues. For a higher strain stiffening level (i.e., $\mathcal{J}_m > 21$), the maximum critical growth ratio $\bar{\mathcal{G}}_{\max}$ tends to conform to the neo-Hookean model calculations. For biological tissues with a moderate strain stiffening level (such as $0.46 < \mathcal{J}_m < 21$), the strain-stiffening effect causes a noteworthy postponement in the onset of growth instability in the system. Finally, when the tissue is stiffened under very low strain (i.e., $\mathcal{J}_m < 0.46$), the onset of growth instability is prevented, resulting in the retention of a smooth hyperelastic cylindrical tubular structure. This suggests that an unstable morphology never forms and that the epithelial tissue remains smooth at all levels of growth. It is therefore safe to assume that multifactorial control, including strain stiffening, greatly expands the scope for pattern selection for morphological instability in biological tissues.

Finally, while some researchers reason that various aspects of airway remodeling may not confer significant benefits to the host, we contend that certain aspects of such remodeling do in fact have advantageous effects. Notably, the thickening of the airway's reticular basement membrane results in increased stiffness of the airway wall (Mostaço-Guidolin et al., 2019), which in turn reduces airway obstruction by mitigating mucosal folding during smooth muscle contraction. However, note that both reticular basement membrane thickening and stiffening of the airway wall are epiphenomena of strain-stiffening-induced delayed instability. Our computational results provide valuable insights into patterning emergence and predictive models of airway remodeling, despite not delving into subcellular processes.

Declaration of competing interest

The authors declare that they have no known competing financial interests or personal relationships that could have appeared to influence the work reported in this paper.

Data availability

Data will be made available on request.

Acknowledgments

Appendix A. Supplementary data

Supplementary material related to this article can be found online at https://doi.org/10.1016/j.jmps.2023.105360.

References

Amar, M.B., Goriely, A., 2005. Growth and instability in elastic tissues. J. Mech. Phys. Solids 53 (10), 2284–2319.

Bayly, P., Taber, L., Kroenke, C., 2014. Mechanical forces in cerebral cortical folding: a review of measurements and models. J. Mech. Behav. Biomed. Mater. 29, 568–581.

Ben Amar, M., Jia, F., 2013. Anisotropic growth shapes intestinal tissues during embryogenesis. Proc. Natl. Acad. Sci. USA 110 (26), 10525–10530.

Black, J.L., Roth, M., Lee, J., Carlin, S., Johnson, P.R., 2001. Mechanisms of airway remodeling: airway smooth muscle. Am. J. Resp. Crit. Care. 164 (supplement_2), S63–S66.

Braeu, F.A., Aydin, R.C., Cyron, C.J., 2019. Anisotropic stiffness and tensional homeostasis induce a natural anisotropy of volumetric growth and remodeling in soft biological tissues. Biomech. Model. Mechanobiol. 18 (2), 327–345.

Budday, S., Steinmann, P., Kuhl, E., 2014. The role of mechanics during brain development. J. Mech. Phys. Solids 72, 75–92.

Ciarletta, P., Balbi, V., Kuhl, E., 2014. Pattern selection in growing tubular tissues. Phys. Rev. Lett. 113 (24), 248101.

Ciarletta, P., Destrade, M., Gower, A.L., 2016. On residual stresses and homeostasis: an elastic theory of functional adaptation in living matter. Sci. Rep. 6 (1), 1–8.

Ciarletta, P., Pozzi, G., Riccobelli, D., 2022. The Föppl–von Kármán equations of elastic plates with initial stress. R. Soc. Open Sci. 9 (5), 220421.

Das, R.K., Gocheva, V., Hammink, R., Zouani, O.F., Rowan, A.E., 2016. Stress-stiffening-mediated stem-cell commitment switch in soft responsive hydrogels. Nature Mater. 15 (3), 318–325.

Dervaux, J., Amar, M.B., 2011. Buckling condensation in constrained growth. J. Mech. Phys. Solids 59 (3), 538–560.

Destrade, M., Annaidh, A.N., Coman, C.D., 2009. Bending instabilities of soft biological tissues. Int. J. Solids Struct. 46 (25–26), 4322–4330.

Doherty, T.A., Soroosh, P., Khorram, N., Fukuyama, S., Rosenthal, P., Cho, J.Y., Norris, P.S., Choi, H., Scheu, S., Pfeffer, K., et al., 2011. The tumor necrosis factor family member LIGHT is a target for asthmatic airway remodeling. Nature Med. 17 (5), 596–603.

Du, Y., Lü, C., Chen, W., Destrade, M., 2018. Modified multiplicative decomposition model for tissue growth: beyond the initial stress-free state. J. Mech. Phys. Solids 118, 133–151.

Du, Y., Lü, C., Destrade, M., Chen, W., 2019a. Influence of initial residual stress on growth and pattern creation for a layered aorta. Sci. Rep. 9 (1), 8232.

Du, Y., Lü, C., Liu, C., Han, Z., Li, J., Chen, W., Qu, S., Destrade, M., 2019b. Prescribing patterns in growing tubular soft matter by initial residual stress. Soft Matter 15 (42), 8468–8474.

Du, Y., Su, Y., Lü, C., Chen, W., Destrade, M., 2020. Electro-mechanically guided growth and patterns. J. Mech. Phys. Solids 143, 104073.

Dumais, J., 2007. Can mechanics control pattern formation in plants? Curr. Opin. Plant Biol. 10 (1), 58–62.

Eskandari, M., Kuhl, E., 2015. Systems biology and mechanics of growth. Wiley Interdiscip. Rev. Syst. Biol. Med. 7 (6), 401–412.

Fuiman, L., 1983. Growth gradients in fish larvae. J. Fish Biol. 23 (1), 117–123.

Goriely, A., 2017. The Mathematics and Mechanics of Biological Growth, vol. 45. Springer.

Gower, A., Ciarletta, P., Destrade, M., 2015. Initial stress symmetry and its applications in elasticity. Proc. R. Soc. Lond. Ser. A Math. Phys. Eng. Sci. 471 (2183), 20150448.

Hirota, N., Martin, J.G., 2013. Mechanisms of airway remodeling. Chest 144 (3), 1026–1032.

Hoger, A., 1997. Virtual configurations and constitutive equations for residually stressed bodies with material symmetry. J. Elasticity 48, 125–144.

Hough, K.P., Curtiss, M.L., Blain, T.J., Liu, R.-M., Trevor, J., Deshane, J.S., Thannickal, V.J., 2020. Airway remodeling in asthma. Front. Med. 7, 191.

Jamieson, R.R., Stasiak, S.E., Polio, S.R., Augspurg, R.D., McCormick, C.A., Ruberti, J.W., Parameswaran, H., 2021. Stiffening of the extracellular matrix is a sufficient condition for airway hyperreactivity. J. Appl. Physiol..

Jaspers, M., Dennison, M., Mabesoone, M.F., MacKintosh, F.C., Rowan, A.E., Kouwer, P.H., 2014. Ultra-responsive soft matter from strain-stiffening hydrogels. Nature Commun. 5 (1), 5808.

Jin, L., Suo, Z., 2015. Smoothening creases on surfaces of strain-stiffening materials. J. Mech. Phys. Solids 74, 68–79.

Kouwer, P.H., Koepf, M., Le Sage, V.A., Jaspers, M., Van Buul, A.M., Eksteen-Akeroyd, Z.H., Woltinge, T., Schwartz, E., Kitto, H.J., Hoogenboom, R., et al., 2013. Responsive biomimetic networks from polyisocyanopeptide hydrogels. Nature 493 (7434), 651–655.

Lee, T., Holland, M.A., Weickenmeier, J., Gosain, A.K., Tepole, A.B., 2021. The geometry of incompatibility in growing soft tissues: Theory and numerical characterization. J. Mech. Phys. Solids 146, 104177.

Lin, S., Mao, Y., Yuk, H., Zhao, X., 2018. Material-stiffening suppresses elastic fingering and fringe instabilities. Int. J. Solids Struct. 139, 96–104.

Liu, C., Du, Y., Li, K., Zhang, Y., Han, Z., Zhang, Y., Qu, S., Lü, C., 2022. Geometrical incompatibility guides pattern selection in growing bilayer tubes. J. Mech. Phys. Solids 169, 105087.

Lubarda, V.A., Hoger, A., 2002. On the mechanics of solids with a growing mass. Int. J. Solids Struct. 39 (18), 4627–4664.

Menzel, A., 2005. Modelling of anisotropic growth in biological tissues: a new approach and computational aspects. Biomech. Model. Mechanobiol. 3, 147–171.

Mostaço-Guidolin, L.B., Osei, E.T., Ullah, J., Hajimohammadi, S., Fouadi, M., Li, X., Li, V., Shaheen, F., Yang, C.X., Chu, F., et al., 2019. Defective fibrillar collagen organization by fibroblasts contributes to airway remodeling in asthma. Am. J. Resp. Crit. Care. 200 (4), 431–443.

Moulton, D., Goriely, A., 2011. Circumferential buckling instability of a growing cylindrical tube. J. Mech. Phys. Solids 59 (3), 525–537.

Riccobelli, D., Bevilacqua, G., 2020. Surface tension controls the onset of gyrification in brain organoids. J. Mech. Phys. Solids 134, 103745.

Rodrigo-Navarro, A., Sankaran, S., Dalby, M.J., del Campo, A., Salmeron-Sanchez, M., 2021. Engineered living biomaterials. Nat. Rev. Mater. 6 (12), 1175–1190.

Rodriguez, E.K., Hoger, A., McCulloch, A.D., 1994. Stress-dependent finite growth in soft elastic tissues. J. Biomech. 27 (4), 455–467.

Rolland-Lagan, A.-G., Bangham, J.A., Coen, E., 2003. Growth dynamics underlying petal shape and asymmetry. Nature 422 (6928), 161–163.

Sharma, A., Licup, A., Jansen, K., Rens, R., Sheinman, M., Koenderink, G., MacKintosh, F., 2016. Strain-controlled criticality governs the nonlinear mechanics of fibre networks. Nat. Phys. 12 (6), 584–587.

Shyer, A.E., Tallinen, T., Nerurkar, N.L., Wei, Z., Gil, E.S., Kaplan, D.L., Tabin, C.J., Mahadevan, L., 2013. Villification: how the gut gets its villi. Science 342 (6155), 212–218.

Skalak, R., Zargaryan, S., Jain, R.K., Netti, P.A., Hoger, A., 1996. Compatibility and the genesis of residual stress by volumetric growth. J. Math. Biol. 34, 889–914.

Soleimani, M., Muthyala, N., Marino, M., Wriggers, P., 2020. A novel stress-induced anisotropic growth model driven by nutrient diffusion: theory, FEM implementation and applications in bio-mechanical problems. J. Mech. Phys. Solids 144, 104097.

Storm, C., Pastore, J.J., MacKintosh, F.C., Lubensky, T.C., Janmey, P.A., 2005. Nonlinear elasticity in biological gels. Nature 435 (7039), 191–194.

Taber, L.A., 1995. Biomechanics of growth, remodeling, and morphogenesis. Appl. Mech. Rev. 48 (8), 487–545.

Tagaya, E., Tamaoki, J., 2007. Mechanisms of airway remodeling in asthma. Allergol. Int. 56 (4), 331–340.

Varricchi, G., Ferri, S., Pepys, J., Poto, R., Spadaro, G., Nappi, E., Paoletti, G., Virchow, J.C., Heffler, E., Canonica, W.G., 2022. Biologics and airway remodeling in severe asthma. Allergy 77 (12), 3538–3552.

Vatankhah-Varnosfaderani, M., Daniel, W.F., Everhart, M.H., Pandya, A.A., Liang, H., Matyjaszewski, K., Dobrynin, A.V., Sheiko, S.S., 2017. Mimicking biological stress–strain behaviour with synthetic elastomers. Nature 549 (7673), 497–501.

Wang, T., Dai, Z., Potier-Ferry, M., Xu, F., 2023. Curvature-regulated multiphase patterns in Tori. Phys. Rev. Lett. 130 (4), 048201.

Wang, Y., Wang, C., 2021. Buckling of ultrastretchable kirigami metastructures for mechanical programmability and energy harvesting. Int. J. Solids Struct. 213, 93–102.

Wang, Y., Wang, C., 2022. Mechanics of strain-limiting wrinkled kirigami for flexible devices: High flexibility, stretchability and compressibility. Int. J. Solids Struct. 238, 111382.

Weickenmeier, J., Kurt, M., Ozkaya, E., de Rooij, R., Ovaert, T.C., Ehman, R., Pauly, K.B., Kuhl, E., 2018. Brain stiffens post mortem. J. Mech. Behav. Biomed. Mater. 84, 88–98.

Xia, T., Zheng, W., Lure, F., Guan, Y., 2021. CT phenotypes in mild-to-moderate chronic obstructive pulmonary disease: difference before and after the age of 60 years. Clin. Radiol. 76 (4), 273–280.

Xu, F., Fu, C., Yang, Y., 2020. Water affects morphogenesis of growing aquatic plant leaves. Phys. Rev. Lett. 124 (3), 038003.

Xu, F., Huang, Y., Zhao, S., Feng, X.-Q., 2022. Chiral topographic instability in shrinking spheres. Nat. Comput. Sci. 2 (10), 632–640.

Xue, S.-L., Li, B., Feng, X.-Q., Gao, H., 2016. Biochemomechanical poroelastic theory of avascular tumor growth. J. Mech. Phys. Solids 94, 409–432.